

CERN-PH-EP-2014-083
06 May 2014

Azimuthal anisotropy of D meson production in Pb–Pb collisions at $\sqrt{s_{NN}} = 2.76$ TeV

The ALICE Collaboration*

Abstract

The production of the prompt charm mesons D^0 , D^+ and D^{*+} relative to the reaction plane was measured in Pb–Pb collisions at a centre-of-mass energy per nucleon–nucleon collision of $\sqrt{s_{NN}} = 2.76$ TeV with the ALICE detector at the LHC. D mesons were reconstructed via their hadronic decays at central rapidity in the transverse momentum (p_T) interval 2–16 GeV/ c . The azimuthal anisotropy is quantified in terms of the second coefficient v_2 in a Fourier expansion of the D meson azimuthal distribution, and in terms of the nuclear modification factor R_{AA} , measured in the direction of the reaction plane and orthogonal to it. v_2 was measured with three different methods and in three centrality classes in the interval 0–50%. A positive v_2 is observed in mid-central collisions (30–50% centrality class), with a value of about 0.2 in the interval $2 < p_T < 6$ GeV/ c , which decreases towards more central collisions (10–30% and 0–10% classes). The positive v_2 is also reflected in the nuclear modification factor, which shows a stronger suppression in the direction orthogonal to the reaction plane for mid-central collisions. The measurements are compared to theoretical calculations of charm quark transport and energy loss in high-density strongly-interacting matter at high temperature. The models that include substantial elastic interactions with an expanding medium provide a good description of the observed anisotropy. However, they are challenged to simultaneously describe the strong suppression of high- p_T yield of D mesons in central collisions and their azimuthal anisotropy in non-central collisions.

*See Appendix A for the list of collaboration members

1 Introduction

Collisions of heavy nuclei at ultra-relativistic energies are expected to lead to the formation of a high-density colour-deconfined state of strongly-interacting matter. According to calculations of Quantum Chromo-Dynamics (QCD) on the lattice (see e.g. [1–4]), a phase transition to the Quark–Gluon Plasma (QGP) state can occur in these collisions, when conditions of high energy density and temperature are reached. Heavy quarks (charm and beauty), with large masses $m_c \approx 1.3$ and $m_b \approx 4.5$ GeV/ c^2 , are produced in pairs predominantly at the initial stage of the collision [5] in hard scattering processes characterized by timescales shorter than the medium formation time. They traverse the medium and interact with its constituents via both inelastic (medium-induced gluon radiation, i.e. radiative energy loss) [6, 7] and elastic (collisional) [8] QCD processes. Heavy-flavour hadrons are thus effective probes of the properties of the medium formed in the collisions.

Compelling evidence for heavy-quark energy loss in strongly-interacting matter is provided by the observation of a modification of the transverse momentum (p_T) distributions of heavy-flavour hadrons. This modification is quantified by the nuclear modification factor $R_{AA}(p_T) = dN_{AA}/dp_T / \langle T_{AA} \rangle d\sigma_{pp}/dp_T$, where dN_{AA}/dp_T is the differential yield in nucleus–nucleus collisions in a given centrality class, $d\sigma_{pp}/dp_T$ is the cross section in pp collisions, and $\langle T_{AA} \rangle$ is the average nuclear overlap function [9]. In central nucleus–nucleus collisions at RHIC and LHC energies, R_{AA} values significantly below unity were observed for heavy-flavour hadrons with p_T values larger than a few GeV/ c [10–14]. A suppression by a factor up to 3–5 ($R_{AA} \approx 0.25$) at $p_T \simeq 5$ GeV/ c was measured in central collisions for inclusive electrons and muons from heavy-flavour hadron decays, both at RHIC ($\sqrt{s_{NN}} = 200$ GeV), by the PHENIX and STAR Collaborations [10, 11], and at the LHC ($\sqrt{s_{NN}} = 2.76$ TeV), by the ALICE Collaboration [13]. At the LHC, the effect was also measured separately for charm, via D mesons by the ALICE Collaboration [12], and for beauty, via non-prompt J/ψ particles from B hadron decays by the CMS Collaboration [14].

The D meson suppression at the LHC is described (see e.g. [12]) by model calculations that implement a combination of mechanisms of heavy-quark interactions with the medium, via radiative and collisional processes, as well as in-medium formation and dissociation of charm hadrons [15–21]. Model comparisons with more differential measurements can provide important insights into the relevance of the various interaction mechanisms and the properties of the medium. In particular, the dependence of the partonic energy loss on the in-medium path length is expected to be different for each mechanism (linear for collisional processes [8] and close to quadratic for radiative processes [7]). In addition, it is an open question whether low-momentum heavy quarks participate, through interactions with the medium, in the collective expansion of the system and whether they can reach thermal equilibrium with the medium constituents [22, 23]. It was also suggested that low-momentum heavy quarks could hadronize not only via fragmentation in the vacuum, but also via the mechanism of recombination with other quarks from the medium [23, 24].

These questions can be addressed with azimuthal anisotropy measurements of heavy-flavour hadron production with respect to the reaction plane, defined by the beam axis and the impact parameter of the collision. For non-central collisions, the two nuclei overlap in an approximately lenticular region, the short axis of which lies in the reaction plane. Hard partons are produced at an early stage, when the geometrical anisotropy is not yet reduced by the system expansion. Therefore, partons emitted in the direction of the reaction plane (in-plane) have, on average, a shorter in-medium path length than partons emitted orthogonally (out-of-plane), leading *a priori* to a stronger high- p_T suppression in the latter case. In the low-momentum region, the in-medium interactions can also modify the parton emission directions, thus translating the initial spatial anisotropy into a momentum anisotropy of the final-state particles. Both effects cause a momentum anisotropy that can be characterized with the coefficients v_n and the symmetry planes Ψ_n of the Fourier expansion of the p_T -dependent particle distribution $d^2N/dp_T d\phi$ in azimuthal angle ϕ . The elliptic flow is the second Fourier coefficient v_2 , which can also be expressed as the average

over all particles in all events of the angular correlation $\cos[2(\varphi - \Psi_2)]$. If the distribution of the matter inside the nuclei were smooth, the symmetry planes Ψ_n of all harmonics for spherically symmetric nuclei would coincide with the reaction plane. Due to fluctuations in the positions of the participant nucleons, the plane of symmetry fluctuates event-by-event around the reaction plane, independently for each harmonic, so that the Ψ_n directions no longer coincide.

A path-length dependent energy loss, which gives a positive v_2 , is considered to be the dominant contribution to the azimuthal anisotropy of charged hadrons in the high p_T region, above 8–10 GeV/c [28, 29]. At low p_T , a large v_2 is considered as an evidence for the collective hydrodynamical expansion of the medium [30, 31]. Measurements of light-flavour hadron v_2 over a large p_T range at RHIC and LHC are generally consistent with these expectations [17, 32–38]. In contrast to light quarks and gluons, which can be produced or annihilated during the entire evolution of the medium, heavy quarks are produced predominantly in initial hard scattering processes and their annihilation rate is small [5]. Thus, the final state heavy-flavour hadrons at all transverse momenta originate from heavy quarks that experienced each stage of the system evolution. High-momentum heavy quarks quenched by in-medium energy loss are shifted towards low momenta and, while participating in the collective expansion, they may ultimately thermalize in the system. In this context, the measurement of D meson v_2 is also important for the interpretation of recent results on J/ψ anisotropy [25], because J/ψ mesons formed from $c\bar{c}$ recombination would inherit the azimuthal anisotropy of their constituent quarks [26, 27].

An azimuthal anisotropy in heavy-flavour production was observed in Au–Au collisions at RHIC with v_2 values of up to about 0.13 for electrons from heavy-flavour decays [39]. The measured asymmetry is reproduced by several models [18–20, 40–45] implementing heavy-quark transport within a medium that undergoes a hydrodynamical expansion. The transport properties, i.e. the diffusion coefficients, of heavy quarks in the medium can be related to its shear viscosity [40]. For LHC energies these models predict a large v_2 (in the range 0.10–0.20 in semi-central collisions) for D mesons at $p_T \approx 2\text{--}3$ GeV/c and a decrease to a constant value $v_2 \approx 0.05$ at high p_T . The models described in Refs. [19, 42–45] include, at the hadronization stage, a contribution from the recombination of charm quarks with light quarks from the medium, which enhances v_2 at low p_T .

The measurement of the D meson v_2 in the centrality class 30–50% in Pb–Pb collisions at $\sqrt{s_{NN}} = 2.76$ TeV, carried out using the ALICE detector, was presented in [46]. v_2 was found to be significantly larger than zero in the interval $2 < p_T < 6$ GeV/c and comparable in magnitude with that of charged particles.

Here the measurement is extended to other centrality classes and accompanied with a study of the azimuthal dependence of the nuclear modification factor. The decays $D^0 \rightarrow K^- \pi^+$, $D^+ \rightarrow K^- \pi^+ \pi^+$ and $D^{*+} \rightarrow D^0 \pi^+$ and charge conjugates were reconstructed. The v_2 coefficient was measured with various methods in the centrality class 30–50% as a function of p_T . For the D^0 meson, which has the largest statistical significance, the centrality dependence of v_2 in the range 0–50% is presented and the anisotropy is also quantified in terms of the nuclear modification factor R_{AA} in two 90°-wide azimuthal intervals centred around the in-plane and out-of-plane directions.

The experimental apparatus is presented in Section 2. The data analysis is described in Section 3, including the data sample, the D meson reconstruction and the anisotropy measurement methods. Systematic uncertainties are discussed in Section 4. The results on v_2 and R_{AA} are presented in Section 5 and compared with model calculations in Section 6.

2 Experimental apparatus

The ALICE apparatus is described in [47]. In this section, the characteristics of the detectors used for the D meson analyses are summarized. The z -axis of the ALICE coordinate system is defined by the beam

94 direction, the x -axis lies in the horizontal plane and is pointing towards the centre of the LHC accelerator
95 ring and the y -axis is pointing upward.

96 Charged-particle tracks are reconstructed in the central pseudo-rapidity region ($|\eta| < 0.9$) with the Time
97 Projection Chamber (TPC) and the Inner Tracking System (ITS). For this analysis, charged hadron
98 identification was performed using information from the TPC and the Time Of Flight (TOF) detectors.
99 These detectors are located inside a large solenoidal magnet that provides a field with a strength of 0.5 T,
100 parallel to the beam direction. Two VZERO scintillator detectors, located in the forward and backward
101 pseudo-rapidity regions, are used for online event triggering, collision centrality determination and, along
102 with the Zero Degree Calorimeter (ZDC), for offline event selection.

103 The ITS [48] includes six cylindrical layers of silicon detectors surrounding the beam vacuum tube, at
104 radial distances from the nominal beam line ranging from 3.9 cm for the innermost layer to 43 cm for
105 the outermost one. The two innermost layers consist of Silicon Pixel Detectors (SPD) with a pixel size
106 of $50 \times 425 \mu\text{m}^2$ ($r\phi \times z$, in cylindrical coordinates), providing an intrinsic spatial resolution of $12 \mu\text{m}$
107 in $r\phi$ and $100 \mu\text{m}$ in z . The third and fourth layers use Silicon Drift Detectors (SDD) with an intrinsic
108 spatial resolution of $35 \mu\text{m}$ and $25 \mu\text{m}$ in $r\phi$ and z , respectively. The two outermost layers of the ITS
109 contain double-sided Silicon Strip Detectors (SSD) with an intrinsic spatial resolution of $20 \mu\text{m}$ in $r\phi$
110 and $830 \mu\text{m}$ in the z -direction. The alignment of the ITS sensor modules is crucial for the precise space
111 point reconstruction needed for the heavy-flavour analyses. It was performed using survey information,
112 cosmic-ray tracks and pp data. A detailed description of the employed methods can be found in [48].
113 The effective spatial resolution along the most precise direction, $r\phi$, is about 14, 40 and $25 \mu\text{m}$, for SPD,
114 SDD and SSD, respectively [48, 49].

115 The TPC [50] covers the pseudo-rapidity interval $|\eta| < 0.9$ and extends in radius from 85 cm to 247 cm.
116 Charged-particle tracks are reconstructed and identified with up to 159 space points. The transverse
117 momentum resolution for tracks reconstructed with the TPC and the ITS ranges from about 1% at
118 $p_T = 1 \text{ GeV}/c$ to about 2% at $10 \text{ GeV}/c$, both in pp and Pb–Pb collisions. The TPC also provides a
119 measurement of the specific energy deposition dE/dx , with up to 159 samples. The truncated mean
120 method, using only the lowest 60% of the measured dE/dx samples, gives a Gaussian distribution with
121 a resolution (ratio of sigma over centroid) of about 6%, which is slightly dependent on the track quality
122 and on the detector occupancy.

123 The TOF detector [51] is positioned at a radius of 370–399 cm and it has the same pseudo-rapidity
124 coverage as the TPC ($|\eta| < 0.9$). The TOF provides an arrival time measurement for charged tracks with
125 an overall resolution, including the measurement of the event start time, of about 80 ps for pions and
126 kaons at $p_T = 1 \text{ GeV}/c$ in the Pb–Pb collision centrality range used in this analysis [51].

127 The VZERO detector [52] consists of two arrays of scintillator counters covering the pseudo-rapidity
128 regions $-3.7 < \eta < -1.7$ (VZERO-C) and $2.8 < \eta < 5.1$ (VZERO-A). Each array is composed of
129 8×4 segments in the azimuthal and radial directions, respectively. This detector provides a low-bias
130 interaction trigger (see Section 3.1). For Pb–Pb collisions, the signal amplitude from its segments is used
131 to classify events according to centrality, while the azimuthal segmentation allows for an estimation of
132 the reaction plane.

133 The ZDCs are located on either side of the interaction point at $z \approx \pm 114 \text{ m}$. The timing information
134 from the neutron ZDCs was used to reject parasitic collisions between one of the two beams and residual
135 nuclei present in the vacuum tube.

Table 1: Number of events and integrated luminosity for the considered centrality classes, expressed as percentiles of the hadronic cross section. The uncertainty on the integrated luminosity derives from the uncertainty of the hadronic Pb–Pb cross section from the Glauber model [9, 53].

Centrality class	N_{events}	$L_{\text{int}} (\mu\text{b}^{-1})$
0–10%	16.0×10^6	20.9 ± 0.7
10–30%	9.5×10^6	6.2 ± 0.2
30–50%	9.5×10^6	6.2 ± 0.2

136 3 Data analysis

137 3.1 Data sample and event selection

138 The analysis was performed on a data sample of Pb–Pb collisions recorded in November and December
 139 2011 at a centre-of-mass energy per nucleon–nucleon collision of $\sqrt{s_{\text{NN}}} = 2.76$ TeV. The events were
 140 collected with an interaction trigger based on information from the VZERO detector, which required
 141 coincident signals recorded in the detectors at forward and backward pseudo-rapidities. An online
 142 selection based on the VZERO signal amplitude was used to enhance the sample of central and mid-
 143 central collisions through two separate trigger classes. Events were further selected offline to remove
 144 background coming from parasitic beam interactions by using the time information provided by the
 145 VZERO and the neutron ZDC detectors. Only events with a reconstructed interaction point (primary
 146 vertex), determined by extrapolating charged-particle tracks, within ± 10 cm from the centre of the
 147 detector along the beam line were used in the analysis.

148 Collisions were classified in centrality classes, determined from the sum of the amplitudes of the signals
 149 in the VZERO detector and defined in terms of percentiles of the total hadronic Pb–Pb cross section. In
 150 order to relate the centrality classes to the collision geometry, the distribution of the VZERO summed
 151 amplitudes was fitted by a model based on the Glauber approach for the geometrical description of
 152 the nuclear collision [9] complemented by a two-component model for particle production [53]. The
 153 centrality classes used in the analysis are reported in Table 1, together with the number of events in each
 154 class and the corresponding integrated luminosity.

155 3.2 D meson reconstruction

156 The D^0 , D^+ and D^{*+} mesons and their antiparticles were reconstructed in the rapidity interval $|y| < 0.8$
 157 via their hadronic decay channels $D^0 \rightarrow K^- \pi^+$ (with branching ratio, BR, of $3.88 \pm 0.05\%$), $D^+ \rightarrow K^- \pi^+ \pi^+$
 158 (BR = $9.13 \pm 0.19\%$), and $D^{*+} \rightarrow D^0 \pi^+$ (BR = $67.7 \pm 0.5\%$) and their corresponding charge conju-
 159 gates [54]. The D^0 and D^+ mesons decay weakly with mean proper decay lengths ($c\tau$) of approximately
 160 123 and 312 μm [54]. The D^{*+} meson decays strongly at the primary vertex.

161 D^0 and D^+ candidates were defined from pairs and triplets of tracks within the fiducial acceptance
 162 $|\eta| < 0.8$, selected by requiring at least 70 associated space points in the TPC, $\chi^2/\text{ndf} < 2$ for the
 163 momentum fit, and at least two associated hits in the ITS, with at least one of them in the SPD. A
 164 transverse momentum threshold $p_{\text{T}} > 0.4$ GeV/ c was applied in order to reduce the combinatorial
 165 background. D^{*+} candidates were obtained by combining the D^0 candidates with tracks selected with the
 166 same requirements as described above, but with a lower transverse momentum threshold $p_{\text{T}} > 0.1$ GeV/ c
 167 and at least three associated hits in the ITS. The lower p_{T} threshold was used because the momentum of
 168 the pions from D^{*+} decays is typically low, as a consequence of the small mass difference between D^{*+}
 169 and D^0 .

170 The selection of tracks with $|\eta| < 0.8$ introduces a steep drop in the acceptance of D mesons for
 171 rapidities larger than 0.7–0.8, depending on p_{T} . A fiducial acceptance region was, therefore, defined
 172 as: $|y| < y_{\text{fid}}(p_{\text{T}})$, with $y_{\text{fid}}(p_{\text{T}})$ increasing from 0.7 to 0.8 in $2 < p_{\text{T}} < 5$ GeV/ c and taking a constant

173 value of 0.8 for $p_T > 5$ GeV/ c . The D meson v_2 results are not expected to be affected by this small
174 variation in rapidity acceptance.

175 The D meson yields were measured with an invariant mass analysis of reconstructed decays, using
176 kinematic and geometrical selection criteria, and particle identification (PID). The selection of D^0 and
177 D^+ decays was based on the reconstruction of secondary vertices with a separation of a few hundred
178 microns from primary vertex. In the case of the D^{*+} decay, the secondary vertex of the produced D^0
179 was reconstructed. The coordinates of the primary vertex and of the secondary vertices, as well as the
180 corresponding covariance matrices, were computed using a χ^2 minimization method [55].

181 The selection strategy is the same as in previous pp [55, 56] and Pb–Pb [12] analyses. It exploits the
182 displacement of the decay tracks from the primary vertex (transverse impact parameter, d_0), the separa-
183 tion between the secondary and primary vertices (decay length, L) and the pointing of the reconstructed
184 meson momentum to the primary vertex.

185 The transverse impact parameter d_0 of a given track is defined as the signed distance of closest approach
186 of the extrapolated track to the primary vertex in the (x, y) plane. The sign of d_0 is attributed based on
187 the position of the primary vertex with respect to the curve of the (x, y) projection of the track. In Pb–Pb
188 collisions, the impact parameter resolution in the transverse direction is better than $65 \mu\text{m}$ for tracks
189 with a transverse momentum larger than 1 GeV/ c and reaches $20 \mu\text{m}$ for $p_T > 20$ GeV/ c [12]. This
190 includes the contribution from the primary vertex precision, which is better than $10 \mu\text{m}$ in the central
191 and semi-central Pb–Pb events used in this analysis. The impact parameter measurement is significantly
192 less precise along the longitudinal direction, e.g. $170 \mu\text{m}$ at $p_T = 1$ GeV/ c .

193 A pointing condition was applied via a selection on the angle θ_{pointing} between the direction of the
194 reconstructed momentum of the candidate and the straight line connecting the primary and secondary
195 vertices. For Pb–Pb collisions, two additional selection variables were introduced with respect to pp
196 analyses, namely the projection of the pointing angle and of the decay length onto the transverse plane
197 ($\theta_{\text{pointing}}^{xy}$ and L^{xy}). The selection requirements were tuned so as to provide a large statistical significance
198 for the signal and to keep the selection efficiency as high as possible. The chosen selection values depend
199 on the p_T of the D meson and become more stringent from peripheral to central collisions.

200 The selection criteria for the centrality class 30–50% are described in the following. The D^0 candidates
201 were selected by requiring the decay tracks to have an impact parameter significance $|d_0|/\sigma_{d_0} > 0.5$ (σ_{d_0}
202 is the uncertainty on the track impact parameter), and to form a secondary vertex with a track-to-track
203 distance of closest approach smaller than 250–300 μm , depending on p_T , and a decay length larger
204 than 100 μm . The product of the decay track impact parameters, which are of opposite sign for well-
205 displaced signal topologies, was required to be below $-(200 \mu\text{m})^2$ at low p_T (2–3 GeV/ c) and below
206 $-(120 \mu\text{m})^2$ for high p_T candidates (12–16 GeV/ c), with a smooth variation between these values in
207 2–12 GeV/ c . A significance of the projection of the decay length in the transverse plane $L^{xy}/\sigma_{L^{xy}}$ (where
208 $\sigma_{L^{xy}}$ is the uncertainty on L^{xy}) larger than 5 was also required. A selection on the angle θ^* between
209 the kaon momentum in the D^0 rest frame and the boost direction was used to reduce the contamination
210 from background candidates that do not represent real two-body decays and typically have large values
211 of $|\cos \theta^*|$. The selection $|\cos \theta^*| < 0.8$ was applied. The pointing of the D^0 momentum to the primary
212 vertex was implemented by requiring $\cos \theta_{\text{pointing}} > 0.95$ and $\cos \theta_{\text{pointing}}^{xy} > 0.998$ at low p_T (2–3 GeV/ c).
213 Since the background is lower at high p_T , the cuts were progressively made less stringent for increasing
214 p_T . In the 0–10% and 10–30% centrality classes, due to the larger combinatorial background, with
215 respect to the class 30–50%, more stringent selections were applied. The selection criteria applied in the
216 0–10% centrality interval are similar to those used in the 0–20% centrality class in [12].

217 The D^+ candidates were selected by requiring a decay length larger than 1200–1600 μm , depending
218 on p_T , and $\cos \theta_{\text{pointing}}$ larger than 0.998 (0.990) in the p_T interval 3–4 (8–12) GeV/ c , with a smooth
219 variation in-between. Further requirements to reduce the combinatorial background were $\cos \theta_{\text{pointing}}^{xy} >$

220 0.993–0.998 and $L^{xy}/\sigma_{L^{xy}} > 9$ –11, depending on the candidate p_T . In general, the D^+ selection criteria
221 are more stringent than those of the D^0 because of the larger combinatorial background.

222 In the D^{*+} analysis, the selection of the decay D^0 candidates was similar to that used for the D^0 analysis.
223 Only D^0 candidates with invariant mass within 2.5σ of the PDG mass value [54] were used, where σ
224 is the p_T -dependent Gaussian sigma of the invariant mass distribution observed in data. The decay pion
225 was selected with the same track quality criteria as for the D^0 and D^+ decay tracks.

226 Pions and kaons were identified with the TPC and TOF detectors, on the basis of the difference, expressed
227 in units of the resolution (σ), between the measured signal and that expected for the considered particle
228 species. Compatibility regions at $\pm 3\sigma$ around the expected mean energy deposition dE/dx and time-
229 of-flight were used. Tracks without a TOF signal were identified using only the TPC information.
230 This particle identification strategy provided a reduction by a factor of about three of the combinatorial
231 background in the low- p_T range, while preserving most of the signal (see Section 3.4).

232 The D^0 and D^+ raw yields were obtained with a fit to the invariant mass M distribution of the D meson
233 candidates. For the D^{*+} signal the mass difference $\Delta M = M(K^-\pi^+\pi^+) - M(K^-\pi^+)$ was considered.
234 The fit function is the sum of a Gaussian to describe the signal and a term describing the background,
235 which is an exponential for D^0 and D^+ and has the form $f(\Delta M) = a(\Delta M - m_\pi)^b$ for the D^{*+} , where m_π
236 is the charged pion mass and a and b are free parameters. An example of invariant mass distributions
237 is shown in Section 3.3 (Fig. 2). The centroids and the widths of the Gaussian functions were found to
238 be in agreement, respectively, with the D meson PDG mass values [54] and with the simulation results,
239 confirming that the background fluctuations were not causing a distortion in the signal line shape.

240 3.3 Azimuthal anisotropy analysis methods

241 The p_T -differential azimuthal distribution of produced particles can be described by a Fourier series:

$$242 \frac{d^2N}{d\phi dp_T} = \frac{dN}{2\pi dp_T} \left[1 + 2 \sum_{n=1}^{\infty} v_n(p_T) \cos n(\phi - \Psi_n) \right], \quad (1)$$

242 where Ψ_n is the initial state spatial plane of symmetry of the n -th harmonic, defined by the geometrical
243 distribution of the nucleons participating in the collision. In order to determine the second harmonic
244 coefficient v_2 , the \vec{Q} vector

$$245 \vec{Q} = \begin{pmatrix} \sum_{i=1}^N w_i \cos 2\varphi_i \\ \sum_{i=1}^N w_i \sin 2\varphi_i \end{pmatrix} \quad (2)$$

245 is defined from the azimuthal distribution of charged particles, where φ_i are the azimuthal angles and
246 N is the multiplicity of charged particles. The weights w_i are discussed later in the text. The charged
247 particles used for the \vec{Q} vector determination are indicated in the following as reference particles (RFP).
248 The azimuthal angle of the \vec{Q} vector

$$249 \psi_2 = \frac{1}{2} \tan^{-1} \left(\frac{Q_y}{Q_x} \right) \quad (3)$$

249 is called event plane angle and it is an estimate of the second harmonic symmetry plane Ψ_2 .

250 The event plane (EP) [57], scalar product (SP) [58] and two-particle cumulant methods [59] were used
251 to measure the D meson elliptic flow.

252 The charged particle tracks used for the \vec{Q} vector determination were selected with the following criteria:
253 at least 50 associated space points in the TPC; $\chi^2/\text{ndf} < 2$ for the momentum fit in the TPC; a distance
254 of closest approach to the primary vertex smaller than 3.2 cm in z and 2.4 cm in the (x, y) plane. In
255 order to minimize the non-uniformities in the azimuthal acceptance, no requirement was applied on
256 the number of ITS points associated to the track. To avoid auto-correlations between the D meson
257 candidates and the event plane angles, the \vec{Q} vector was calculated for each candidate excluding from the

258 set of reference particles the tracks used to form that particular candidate. Tracks with $p_T > 150$ MeV/ c
 259 were considered and the pseudo-rapidity interval was limited to the positive region $0 < \eta < 0.8$, where
 260 the TPC acceptance and efficiency were more uniform as function of the azimuthal angle for this data
 261 set. The remaining azimuthal non-uniformity was corrected for using weights w_i in Eq. (2), defined as
 262 the inverse of the φ distribution of charged particles used for the \vec{Q} vector determination, $1/(dN/d\varphi_i)$,
 263 multiplied by a function $f(p_T) = \begin{cases} p_T/\text{GeV}/c, & p_T < 2 \text{ GeV}/c \\ 2, & p_T \geq 2 \text{ GeV}/c \end{cases}$. The factor mimics the p_T -dependence of the
 264 charged particle v_2 and it improves the estimate of Ψ_2 by enhancing the contribution of particles with a
 265 stronger flow signal (see e.g. Ref. [35]). The distribution of the event plane angle ψ_2 obtained for this
 266 set of reference particles is shown in the left-hand panel of Fig. 1, for the centrality range 30–50%. The
 267 distribution, divided by its integral, exhibits a residual non-uniformity below 1%.

268 An additional study was performed with the \vec{Q} vector determined from the azimuthal distribution of
 269 signals in the segments of the VZERO detectors, which are sensitive to particles produced at forward
 270 and backward rapidities. The \vec{Q} vector was calculated with Eq. (2), with the sum running over the eight
 271 azimuthal sectors of each VZERO detector, where φ_i was defined by the central azimuth of the i -th
 272 sector, and w_i equal to the signal amplitude in the i -th sector for the selected event, which is proportional
 273 to the number of charged particles crossing the sector. Non-uniformities in the VZERO acceptance and
 274 efficiency were corrected for using the procedure described in [60]. The residual non-uniformity is about
 275 1%, as shown in the left panel of Fig. 1.

276 For the event plane method, the measured anisotropy v_2^{obs} was divided by the event plane resolution
 277 correction factor R_2 according to the equation $v_2 = v_2^{\text{obs}}/R_2$, with R_2 being smaller than one. This
 278 resolution depends on the multiplicity and v_2 of the RFP [57]. For the event plane computed using
 279 TPC tracks, R_2 was determined from the correlation of the event plane angles reconstructed from RFP in
 280 the two sides of the TPC, $-0.8 < \eta < 0$ and $0 < \eta < 0.8$, i.e. two samples of tracks (called sub-events)
 281 with similar multiplicity and v_2 . R_2 is shown in the right-hand panel of Fig. 1 as a function of collision
 282 centrality. The average R_2 values in the three centrality classes used in this analysis are 0.6953 (0–10%),
 283 0.8503 (10–30%) and 0.8059 (30–50%). The statistical uncertainty on R_2 is negligible ($\sim 10^{-4}$). The
 284 systematic uncertainty on R_2 was estimated by using the three-sub-event method described in [61]. In this
 285 case, the event planes reconstructed in the TPC ($0 < \eta < 0.8$), VZERO-A ($2.8 < \eta < 5.1$) and VZERO-
 286 C ($-3.7 < \eta < -1.7$) were used. This method yielded R_2 values smaller than those obtained from the
 287 two-sub-events method by 6.9%, 2.0% and 2.3% for the centrality classes 0–10%, 10–30% and 30–
 288 50%. A part of this difference can be attributed to the presence of short-range non-flow correlations that
 289 are suppressed when the three sub-events with a pseudo-rapidity gap are used. Non-flow correlations
 290 can originate from resonance or cascade-like decays and from jets. The resolution of the event plane
 291 determined from the VZERO detector (summing the signals in VZERO-A and VZERO-C) is also shown
 292 in the right-hand panel of Fig. 1. In this case, R_2 was measured with three sub-events, namely the signals
 293 in the VZERO detector (both A and C sides) and the tracks in the positive and negative η regions of
 294 the TPC. The systematic uncertainty was estimated from the difference with the results obtained with
 295 two TPC sub-events separated by 0.4 units in pseudo-rapidity (η gap). The event plane determination
 296 has a smaller resolution with the VZERO detector than with the TPC tracks. As a consequence, the v_2
 297 measurement is expected to be more precise with the TPC event plane.

298 In the event plane method, the D meson yield was measured in two 90° -wide intervals of $\Delta\varphi = \varphi_D - \psi_2$:
 299 *in-plane* ($-\frac{\pi}{4} < \Delta\varphi \leq \frac{\pi}{4}$ and $\frac{3\pi}{4} < \Delta\varphi \leq \frac{5\pi}{4}$) and *out-of-plane* ($\frac{\pi}{4} < \Delta\varphi \leq \frac{3\pi}{4}$ and $\frac{5\pi}{4} < \Delta\varphi \leq \frac{7\pi}{4}$). φ_D
 300 is defined as the azimuthal angle of the D meson momentum vector at the primary vertex. The invariant
 301 mass distributions for the three meson species are shown in Fig. 2 in three p_T intervals for the 30–50%
 302 centrality class, along with the fits used for the yield estimation (Section 3.2). When fitting the invariant
 303 mass distribution in the two $\Delta\varphi$ intervals, the centroid and the width of the Gaussian functions were
 304 fixed, for each meson species and for each p_T interval, to those obtained from a fit to the invariant mass
 305 distribution integrated over φ , where the statistical significance of the signal is larger.

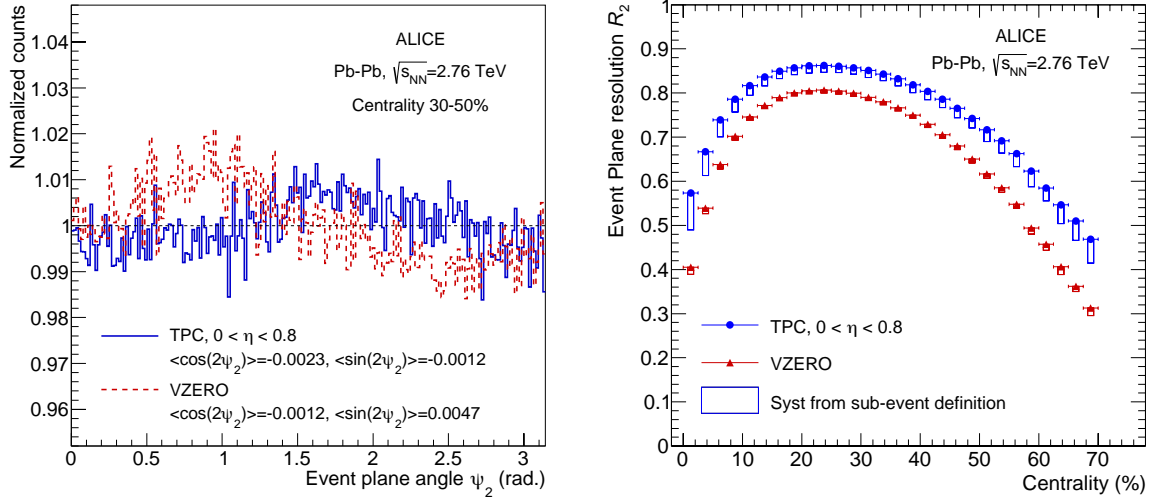


Figure 1: Left: Distribution of event plane angle ψ_2 , estimated from TPC tracks with $0 < \eta < 0.8$ (solid line) or with the VZERO detector signals (dashed line) in the centrality range 30–50%. The distributions are normalized by their integral. Right: Event plane resolution correction factor R_2 as a function of centrality for the TPC and VZERO detectors. The boxes represent the systematic uncertainties estimated from the variation of R_2 when changing the sub-events used for its determination.

306 Integrating Eq. (1) and including the correction for the event plane resolution $1/R_2$ yields:

$$v_2\{\text{EP}\} = \frac{1}{R_2} \frac{\pi}{4} \frac{N_{\text{in-plane}} - N_{\text{out-of-plane}}}{N_{\text{in-plane}} + N_{\text{out-of-plane}}}. \quad (4)$$

307 The contribution of higher harmonics to the v_2 value calculated with this equation can be evaluated by
 308 integrating the corresponding terms of the Fourier series. All odd harmonics, as well as v_4 and v_8 , induce
 309 the same average contribution to $N_{\text{in-plane}}$ and $N_{\text{out-of-plane}}$ due to symmetry, and therefore they do not
 310 affect v_2 calculated with Eq. (4). The contribution of v_6 , v_{10} and higher harmonics is assumed to be
 311 negligible based on the values measured for light-flavour hadrons [62, 63].

312 The measurement of the elliptic flow with the scalar product method is given by [57]:

$$v_2\{\text{SP}\} = \frac{1}{2} \left(\frac{\langle \vec{u}_a \cdot \vec{Q}_b \rangle}{\sqrt{\langle \vec{Q}_a \cdot \vec{Q}_b \rangle}} + \frac{\langle \vec{u}_b \cdot \vec{Q}_a \rangle}{\sqrt{\langle \vec{Q}_a \cdot \vec{Q}_b \rangle}} \right), \quad (5)$$

313 where $\langle \rangle$ indicates an average over D meson candidates in all events. The vector \vec{u} is defined as
 314 $\vec{u} = (\cos 2\varphi_D, \sin 2\varphi_D)$, where φ_D the D meson candidate momentum azimuthal direction. The $\vec{Q}_{a,b}$
 315 and $\vec{u}_{a,b}$ vectors were computed from charged particles and D meson candidates, respectively, in two
 316 separate pseudo-rapidity regions: a) $0 < \eta < 0.8$ and b) $-0.8 < \eta < 0$. The elliptic flow was computed
 317 by correlating D mesons from the positive η region with the charged particles in the negative η region,
 318 and vice versa. This separation in pseudo-rapidity suppresses two-particle correlations at short distance
 319 that are due to decays ($D^* \rightarrow D + X$ and $B \rightarrow D^{(*)} + X$). The denominator in Eq. (5) plays a similar role
 320 as the resolution correction in the event plane method. Since the resolution is proportional to the number
 321 of used RFP, the vectors \vec{Q}_a and \vec{Q}_b were normalized by N_a and N_b , respectively, before averaging over
 322 all events. The azimuthal non-uniformity of the TPC response, which results in non-zero average values
 323 of \vec{Q}_a and \vec{Q}_b , was corrected for using a re-centering procedure [57]: $\vec{Q}'_{a,b} = \vec{Q}_{a,b} - \langle \vec{Q}_{a,b} \rangle$.

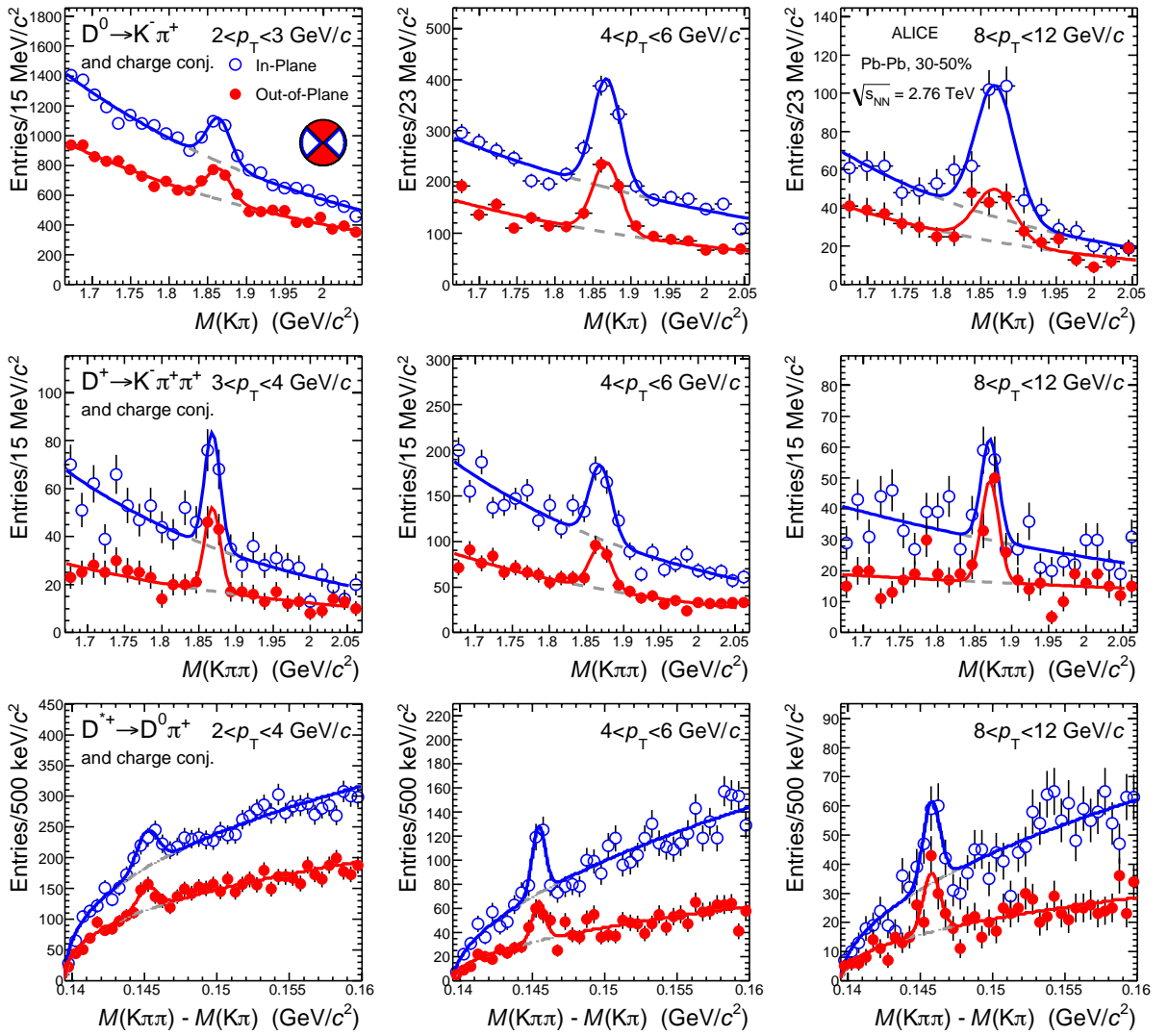


Figure 2: Distributions of the invariant mass for D^0 (upper panels) and D^+ (central panels) candidates and of the mass difference for D^{*+} candidates (lower panels) in the two $\Delta\phi$ intervals used in the event plane method, for Pb–Pb collisions in the 30–50% centrality class. The rapidity interval is $|y| < y_{fid}$ (see Section 3.2 for details). For each meson species three p_T intervals are shown, along with the fits used to extract the signal yield. The definition of the two $\Delta\phi$ intervals is sketched in the top-left panel.

324 The two-particle cumulant is defined by the equation [59, 64, 65]:

$$v_2\{2\} = \frac{\langle \vec{u} \cdot \vec{Q} \rangle}{\sqrt{\langle \frac{\vec{Q}_a \cdot \vec{Q}_b}{N_a \cdot N_b} \rangle}}. \quad (6)$$

325 For this method, the azimuthal non-uniformity of the detector acceptance and efficiency was corrected
 326 for with the aforementioned re-centering procedure. In contrast to the scalar product method, there is no
 327 pseudo-rapidity gap between the D mesons and the RFP for the two-particle cumulant method.

328 For both the scalar product and two-particle cumulant methods, the v_2 of D meson candidates was
 329 computed in narrow intervals of invariant mass M for D^0 and D^+ and mass difference ΔM for the D^{*+} .
 330 In each invariant mass interval, the measured v_2 is the weighted average of the D meson v_2 (v_2^S) and the
 331 background v_2 (v_2^B) with the weights given by the relative fractions of signal (S) and background (B) in

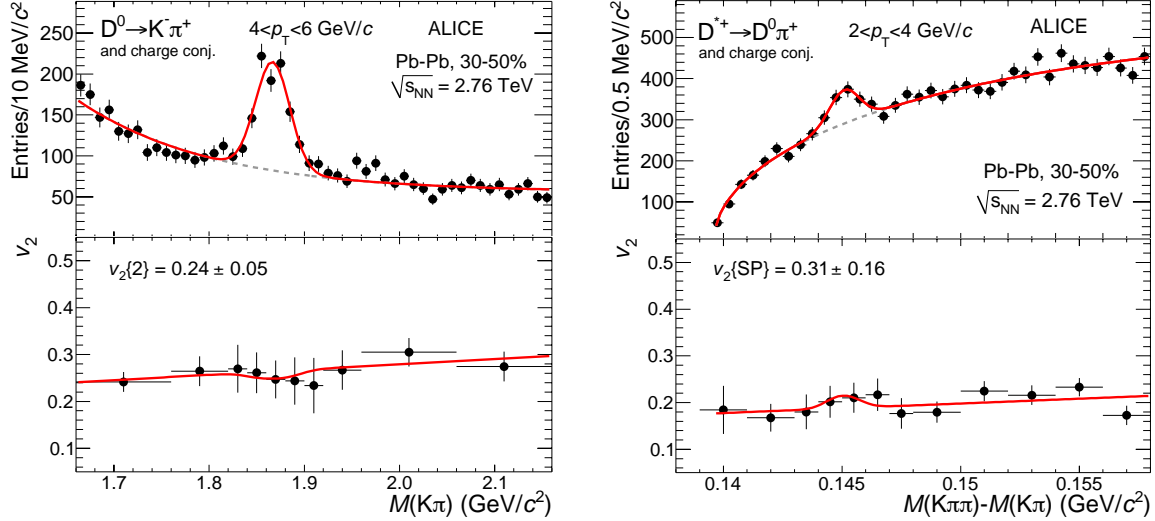


Figure 3: Examples of v_2 extraction with two-particle correlation methods in a selected p_T interval for Pb–Pb collisions in the 30–50% centrality range: the two-particle cumulants method for D^0 (left) and the scalar product method for D^{*+} (right). The lower panels report the D meson v_2 values obtained with the simultaneous fit procedure, as described in the text. The rapidity interval is $|y| < y_{\text{fid}}$ (see Section 3.2 for details).

332 that interval. In order to extract the values of v_2^S and v_2^B , a simultaneous fit of the distributions of counts
 333 and v_2 as a function of invariant mass M was performed. The invariant mass distribution was fitted with
 334 a sum of two terms for signal and background, as explained in Section 3.2. The $v_2(M)$ distribution was
 335 fitted with a function:

$$v_2(M) = [S(M) \cdot v_2^S + B(M) \cdot v_2^B(M)] / [S(M) + B(M)]. \quad (7)$$

336 The background contribution v_2^B was parametrized by a linear function of M . An example of the
 337 corresponding distributions and fits is shown in Fig. 3 for D^0 mesons in the interval $4 < p_T < 6 \text{ GeV}/c$
 338 with the two-particle cumulants method and D^{*+} mesons in the interval $2 < p_T < 4 \text{ GeV}/c$ with the
 339 scalar product method. The values of v_2^S , hereafter indicated as $v_2\{2\}$ and $v_2\{\text{SP}\}$, are also reported in
 340 the figure.

341 Since the measured D meson yield has a feed-down contribution from B meson decays, the measured v_2
 342 is a combination of v_2 of promptly produced and feed-down D mesons. In fact, the contribution of D
 343 mesons from B meson decays is enhanced by the applied selection criteria, because the decay vertices
 344 of the feed-down D mesons are more displaced from the primary vertex. The elliptic flow of promptly
 345 produced D mesons, v_2^{prompt} , can be obtained from the measured v_2^{all} ($v_2\{\text{EP}\}$, $v_2\{2\}$ or $v_2\{\text{SP}\}$) as:

$$v_2^{\text{prompt}} = \frac{1}{f_{\text{prompt}}} v_2^{\text{all}} - \frac{1 - f_{\text{prompt}}}{f_{\text{prompt}}} v_2^{\text{feed-down}}, \quad (8)$$

346 where f_{prompt} is the fraction of promptly produced D mesons in the measured raw yield and $v_2^{\text{feed-down}}$
 347 is the elliptic flow of D mesons from B decays, which depends on the dynamics of beauty quarks in
 348 the medium. These two quantities have not been measured. However, it can be seen in Eq. (8) that
 349 v_2^{all} coincides with v_2^{prompt} if $v_2^{\text{feed-down}} = v_2^{\text{prompt}}$, independent of f_{prompt} . Therefore, the assumption
 350 $v_2^{\text{feed-down}} = v_2^{\text{prompt}}$ was used to compute the central value of the results for the prompt D meson elliptic
 351 flow. Due to the larger mass of the b quark, the v_2 of B mesons is expected to be lower than that of D
 352 mesons. Therefore, the choice of $v_2^{\text{feed-down}} = v_2^{\text{prompt}}$ as central value results to be the most conservative
 353 for the observation of D meson $v_2 > 0$. The details of the systematic uncertainty related to this assumption
 354 are discussed in Section 4.

3.4 Azimuthal dependence of the nuclear modification factor

The in-plane and out-of-plane nuclear modification factors of prompt D^0 mesons are defined as:

$$R_{AA}^{\text{in(out)}}(p_T) = \frac{2 \cdot dN_{AA}^{\text{in(out)}}/dp_T}{\langle T_{AA} \rangle \cdot d\sigma_{pp}/dp_T}, \quad (9)$$

where $dN_{AA}^{\text{in(out)}}/dp_T$ are the D^0 meson per-event yields, integrated over the two 90° -wide intervals used to determine v_2 with the event plane method. The factor 2 in Eq. (9) accounts for the fact that the D meson yields for Pb–Pb collisions are integrated over half of the full azimuth. $R_{AA}^{\text{in(out)}}$ was measured in the 30–50% centrality class for D^0 mesons, which have the highest signal significance, using the yields relative to the event plane defined with TPC tracks in $0 < \eta < 0.8$. The average value of the nuclear overlap function in this centrality class, $\langle T_{AA} \rangle = 3.87 \pm 0.18 \text{ mb}^{-1}$, was determined with the procedure described in [53].

The yields of prompt D^0 mesons in the two azimuthal intervals were obtained as:

$$\left. \frac{dN^{D^0}}{dp_T} \right|_{|y| < 0.5} = \frac{1}{\Delta y \Delta p_T} \frac{f_{\text{prompt}}(p_T) \cdot \frac{1}{2} N_{\text{raw}}^{D^0 + \bar{D}^0}(p_T) \Big|_{|y| < y_{\text{fid}}} \cdot c_{\text{refl}}(p_T)}{(\text{Acc} \times \varepsilon)_{\text{prompt}}(p_T) \cdot \text{BR} \cdot N_{\text{events}}}. \quad (10)$$

The raw yields $N_{\text{raw}}^{D^0 + \bar{D}^0}$ were divided by a factor of two to obtain the charge (particle and antiparticle) averaged yields. The factor $c_{\text{refl}}(p_T)$ was introduced to correct the raw yields for the contribution of signal candidates that are present in the invariant mass distribution both as $D^0 \rightarrow K^- \pi^+$ and as $\bar{D}^0 \rightarrow \pi^- K^+$ (the combination with wrong mass hypothesis assignment is called ‘reflection’). To correct for the contribution of B meson decay feed-down, the raw yields were multiplied by the prompt fraction f_{prompt} , whose determination is described later in this section. Furthermore, they were divided by the product of prompt D meson acceptance and efficiency $(\text{Acc} \times \varepsilon)_{\text{prompt}}$, normalized by the decay channel branching ratio (BR), the transverse momentum (Δp_T) and rapidity ($\Delta y = 2y_{\text{fid}}$) interval widths and the number of events (N_{events}). The normalization by Δy gives the corrected yields in one unit of rapidity $|y| < 0.5$.

The $(\text{Acc} \times \varepsilon)$ correction was determined, as a function of p_T , using Monte Carlo simulations with a detailed description of the ALICE detector geometry and the GEANT3 particle transport package [70]. The simulation was tuned to reproduce the (time-dependent) position and width of the interaction vertex distribution, as well as the number of active electronic channels and the accuracy of the detector calibration. The HIJING v1.383 [69] generator was used to simulate Pb–Pb collisions at $\sqrt{s_{NN}} = 2.76$ TeV and all the produced particles were transported through the detector simulation. Prompt and feed-down D meson signals were added using pp events from the PYTHIA v6.4.21 [68] event generator with the Perugia-0 tune [71]. Each simulated pp event contained a $c\bar{c}$ or $b\bar{b}$ pair with D mesons decaying into the hadronic channels of interest for the analysis. Out of all the particles produced in these PYTHIA pp events, only the heavy-flavour decay products were kept and transported through the detector simulation together with the particles produced by HIJING. In order to minimize the bias on the detector occupancy, the number of D mesons injected into each HIJING event was adjusted according to the Pb–Pb collision centrality.

The efficiencies were evaluated from simulated events that had the same average charged-particle multiplicity, corresponding to the same detector occupancy, as observed for real events in the centrality class 30–50%. Figure 4 shows $(\text{Acc} \times \varepsilon)$ for prompt and feed-down D^0 mesons within the rapidity interval $|y| < y_{\text{fid}}$. The magnitude of $(\text{Acc} \times \varepsilon)$ increases with p_T , starting from about 1% and reaching about 10–15% at high p_T . Also shown in Fig. 4 are the $(\text{Acc} \times \varepsilon)$ values for the case where no PID was applied. The relative difference with respect to the $(\text{Acc} \times \varepsilon)$ obtained using also the PID selection is only about 5%, thus illustrating the high efficiency of the applied PID criteria. The $(\text{Acc} \times \varepsilon)$ for D mesons from B decays is larger than for prompt D mesons by a factor of about 1.5, because the decay vertices of the

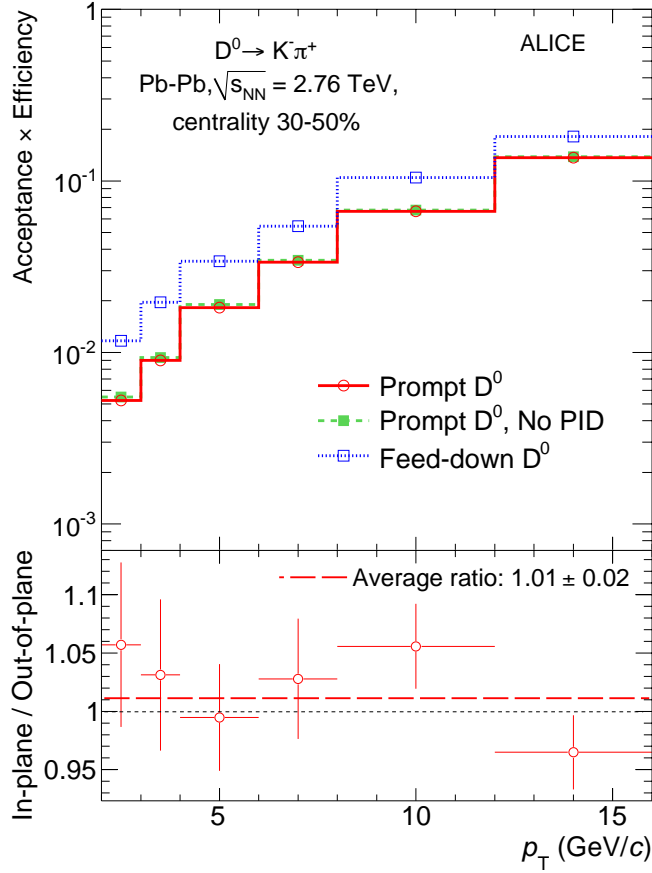


Figure 4: Product of acceptance and efficiency for D^0 mesons in Pb-Pb collisions for 30–50% centrality class (upper panel). The rapidity interval is $|y| < y_{fid}$ (see Section 3.2 for details). The values for prompt (solid lines) and feed-down (dotted lines) D^0 mesons are shown. Also displayed, for comparison, are the values for prompt D^0 mesons without PID selection (dashed lines). The lower panel shows the ratio of the efficiencies for prompt D^0 mesons in the in-plane and out-of-plane regions used for the analysis. This ratio was estimated using simulation samples with a difference in particle multiplicity similar to that observed in data for the two azimuthal regions.

395 feed-down D mesons are more displaced from the primary vertex and are, therefore, more efficiently
 396 selected by the analysis cuts.

397 The possible difference in the reconstruction and selection efficiency between in-plane and out-of-plane
 398 D^0 mesons was studied using simulations. This difference could arise from the variation of the particle
 399 density, and consequently of the detector occupancy, induced by the azimuthal anisotropy of bulk particle
 400 production. The difference in occupancy was estimated in data using the multiplicity of SPD tracklets
 401 in the two considered azimuthal intervals. Tracklets are defined as combinations of two hits in the two
 402 SPD layers that are required to point to the primary vertex. They can be used to measure the multiplicity
 403 of charged particles with $p_T > 50$ MeV/c and $|\eta| < 1.6$. The SPD tracklet multiplicity in the 30–50%
 404 centrality class was found to be larger in-plane than out-of-plane by about 12%. In order to study the
 405 efficiency variation, two sets of simulated events with 12% difference in average multiplicity were used.
 406 The ratio of the two efficiencies was found to be consistent with unity (see lower panel of Fig. 4) and
 407 therefore no correction was applied.

408 The correction factor c_{refl} for the contribution of reflections to the raw yield was determined by including
 409 in the invariant mass fit procedure a template of the distribution of reflected signal candidates, which

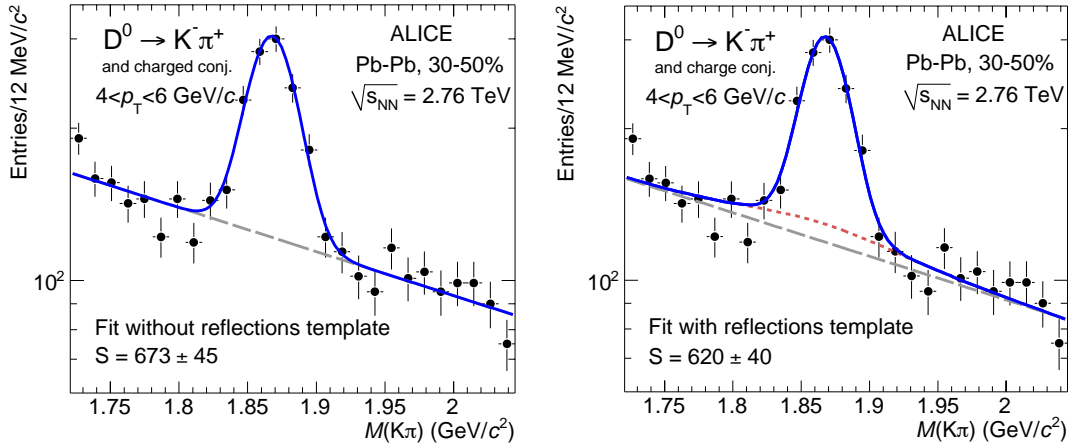


Figure 5: Invariant mass distribution of D^0 candidates with $4 < p_T < 6$ GeV/ c in the centrality class 30–50%: fit without template for reflections, on the left, and with template for reflections (dotted line), on the right. The raw yield obtained as integral of the signal Gaussian function is reported.

410 was obtained from the simulation for each p_T interval. This distribution has a centroid close to the D^0
 411 mass and has typical r.m.s. values of about 100 MeV/ c^2 , i.e. about one order of magnitude larger than the
 412 signal invariant mass resolution. The distribution from the simulation was parametrized with the sum of
 413 two Gaussians, in order to remove the statistical fluctuations. In the fit with the template, the ratio of the
 414 integrals of the total distribution of reflections and of the Gaussian used for the signal were fixed to the
 415 value obtained from the simulation. This ratio is mostly determined by the PID selection, which limits
 416 the probability that a true $K^- \pi^+$ pair can be also compatible with the $\pi^- K^+$ mass hypothesis. For the v_2
 417 analysis described in the previous section, the PID selection was used only for tracks with $p < 4$ GeV/ c .
 418 Since the contribution of the reflections does not depend on the angle relative to the event plane, it is not
 419 necessary to apply the c_{refl} correction for v_2 . For the R_{AA} analysis, in order to minimize the correction,
 420 the PID selection was extended to tracks with $p > 4$ GeV/ c , requiring the compatibility of the TOF and
 421 TPC signals with the expectations for kaons and pions within 3σ . It was verified that this change results
 422 in a variation of v_2 well within the uncertainties. The correction factor c_{refl} was determined as the ratio of
 423 the signal yield from the fit including the reflections template and the signal yield from the fit without the
 424 template. It was computed using the sum of the in-plane and out-of-plane invariant mass distributions, in
 425 order to have a more precise value, and it was applied as in Eq. (10) for both the in-plane and out-of-plane
 426 yields. The procedure was validated using the simulation, where the signal yield obtained from the fit
 427 with the template can be compared with the true signal yield. The numerical value of c_{refl} ranges from
 428 0.98 in the interval $2 < p_T < 3$ GeV/ c to 0.90 in the interval $4 < p_T < 16$ GeV/ c . Figure 5 shows an
 429 example of the fits without (left) and with (right) template for the interval 4–6 GeV/ c .

430 The fraction f_{prompt} of promptly produced D mesons in the measured raw yields was obtained, following
 431 the procedure introduced in [12], as:

$$\begin{aligned}
 f_{\text{prompt}} &= 1 - \frac{N_{\text{raw}}^{D^0 \text{ feed-down}}}{N_{\text{raw}}^{D^0}} = \\
 &= 1 - R_{AA}^{\text{feed-down}} \cdot \langle T_{AA} \rangle \cdot 2 \cdot \left(\frac{d^2 \sigma}{dy dp_T} \right)_{\text{feed-down}}^{\text{FONLL, EvtGen}} \cdot \frac{(\text{Acc} \times \epsilon)_{\text{feed-down}} \cdot \Delta y \Delta p_T \cdot \text{BR} \cdot N_{\text{evt}}}{N_{\text{raw}}^{D^0}}.
 \end{aligned} \tag{11}$$

432 In this expression, where the symbol of the p_T -dependence has been omitted for brevity, $N_{\text{raw}}^{D^0}$ is the
 433 measured raw yield (corrected by the c_{refl} factor) and $N_{\text{raw}}^{D^0 \text{ feed-down}}$ is the contribution of D^0 mesons from
 434 B decays to the raw yield, estimated on the basis of the FONLL calculation of beauty production [72].

In detail, the B meson production cross section in pp collisions at $\sqrt{s} = 2.76$ TeV was folded with the $B \rightarrow D^0 + X$ decay kinematics using EvtGen [73] and multiplied by: the average nuclear overlap function $\langle T_{AA} \rangle$ in the 30–50% centrality class, the acceptance-times-efficiency for feed-down D^0 mesons, and the other factors introduced in Eq. (10). In addition, the nuclear modification factor $R_{AA}^{\text{feed-down}}$ of D mesons from B decays was accounted for. The comparison of the R_{AA} of prompt D mesons [74] with that of J/ψ from B decays [75] measured in the CMS experiment indicates that charmed hadrons are more suppressed than beauty hadrons. Therefore, it was assumed that the ratio of the nuclear modification factors for feed-down and prompt D mesons lies in the range $1 < R_{AA}^{\text{feed-down}}/R_{AA}^{\text{prompt}} < 3$. The value $R_{AA}^{\text{feed-down}} = 2 \cdot R_{AA}^{\text{prompt}}$ was used to compute the correction, and the variation over the full range, which also accounts for possible centrality and p_T dependences, was used to assign a systematic uncertainty. The hypothesis on the nuclear modification of feed-down D mesons was changed with respect the assumption used in [12], based on the most recent results on the R_{AA} of prompt D meson and non-prompt J/ψ mentioned above. As it was done for the v_2 measurement, the feed-down contribution was computed assuming $v_2^{\text{feed-down}} = v_2^{\text{prompt}}$. Therefore, the ratio $R_{AA}^{\text{feed-down}}/R_{AA}^{\text{prompt}}$ is the same in-plane and out-of-plane. The systematic uncertainty related to this assumption is discussed in Section 4. For D^0 mesons, assuming $R_{AA}^{\text{feed-down}} = 2 \cdot R_{AA}^{\text{prompt}}$, the resulting f_{prompt} ranges from about 0.80 in the lowest transverse momentum interval ($2 < p_T < 3$ GeV/c) to about 0.75 at high p_T .

The D^0 yields in the two azimuthal regions with respect to the event plane, obtained from Eq. (10), were corrected for the event plane resolution using the correction factor R_2 (Section 3.3) and the relation given in Eq. (4). For example, the correction factor for the in-plane R_{AA} is $(1 + R_2^{-1})/2 + (N^{\text{in}}/N^{\text{out}}) \cdot (1 - R_2^{-1})/2$, where $N^{\text{in(out)}}$ is the D^0 raw yield. The value $R_2 = 0.8059 \pm 0.0001$ for the 30–50% centrality class and the typical $N^{\text{in}}/N^{\text{out}}$ magnitude result in a correction of approximately +4(–6)% for the in-plane (out-of-plane) yields.

The prompt D^0 meson production cross section in pp collisions used in the calculation of the nuclear modification factor was obtained by scaling the p_T -differential cross section in $|y| < 0.5$ at $\sqrt{s} = 7$ TeV, measured using a data sample of $L_{\text{int}} = 5$ nb $^{-1}$ [55]. The p_T -dependent scaling factor was defined as the ratio of the cross sections obtained from FONLL calculations [72] at $\sqrt{s} = 2.76$ and 7 TeV [76]. The scaled D^0 meson p_T -differential cross section is consistent with that measured at $\sqrt{s} = 2.76$ TeV using a smaller statistics data sample with $L_{\text{int}} = 1.1$ nb $^{-1}$ [56], which only covered a reduced p_T interval with a statistical uncertainty of 20–25% and was therefore not used as pp reference. The correction for reflections was not applied for the D^0 cross section in pp collisions. It was verified that the resulting signal bias is smaller than 5% ($c_{\text{refl}} > 0.95$), which is less than the systematic uncertainty assigned for the yield extraction (10–20% [55]).

4 Systematic uncertainties

Several sources of systematic uncertainty were considered for both v_2 and R_{AA} analyses. The uncertainties on v_2 are described first. Afterwards, the systematic uncertainties affecting R_{AA} in-plane and out-of-plane are discussed. The uncertainties for the 30–50% centrality class are summarized in Tables 2 and 3.

4.1 Uncertainties on v_2

One of the main sources of uncertainty originates from the D meson yield extraction using a fit to the invariant mass distributions. This uncertainty was estimated by repeating the fits under different conditions and by utilizing alternative methods for the yield determination. For the v_2 analysis with the event plane method, the fit ranges and the functional forms for the combinatorial background were varied. Polynomial and exponential functions were tried for D^0 and D^+ background shapes, while a threshold function multiplied by an exponential was considered for the D^{*+} : $a\sqrt{\Delta M - m_\pi} \cdot e^{b(\Delta M - m_\pi)}$, with a and b as free parameters. The D meson yield was also extracted by counting the entries in the invariant

Table 2: Systematic uncertainties on the measurement of v_2 in the 30–50% centrality class for the interval $4 < p_T < 6$ GeV/ c . The uncertainties are comparable in the other p_T intervals.

Particle v_2 analysis	D^0			D^+			D^{*+}		
	$v_2\{\text{EP}\}$	$v_2\{\text{SP}\}$	$v_2\{2\}$	$v_2\{\text{EP}\}$	$v_2\{\text{SP}\}$	$v_2\{2\}$	$v_2\{\text{EP}\}$	$v_2\{\text{SP}\}$	$v_2\{2\}$
M and v_2 fit stability	9%	10%	8%	25%	8%	17%	30%	14%	11%
2 or 3 sub-ev. R_2	2.3%	–	–	2.3%	–	–	2.3%	–	–
R_2 centrality dependence	2%	–	–	2%	–	–	2%	–	–
Centrality selection	–	10%	10%	–	10%	10%	–	10%	10%
Total (excl. B feed-down)	9%	14%	13%	25%	13%	20%	30%	17%	15%
B feed-down		$^{+48}_{-0}\%$			$^{+26}_{-0}\%$			$^{+26}_{-0}\%$	

481 mass distributions after background subtraction. For this procedure the background was estimated with
 482 a fit to the left and right sides of the D meson invariant mass peak (side-band regions), using the fit
 483 functions described in Section 3.2. The v_2 analysis employing the event plane method was performed
 484 by fixing the Gaussian centroids and widths of the in-plane and out-of-plane invariant mass distributions
 485 to the values obtained from a fit of the ϕ -integrated distribution. The analysis was repeated with free
 486 Gaussian parameters in the fit. The systematic uncertainty due to the yield measurement was estimated
 487 as the maximum variation of the v_2 values obtained from the described tests. It amounts to 10–20% for
 488 the D^0 meson, depending on the p_T and centrality intervals, and 20–50% for the D^+ and D^{*+} mesons,
 489 depending on the p_T interval. The same procedure was applied for the two-particle correlation methods
 490 (scalar product and two-particle cumulants), except for the bin counting method and the fixed Gaussian
 491 centroids and widths. Instead, the parametrization of the background $v_2^B(M)$ was varied from a first order
 492 to a second order polynomial. The resulting uncertainty is in the range 15–30%.

493 For the event plane method, two alternative procedures were considered to extract v_2 , which are not
 494 directly based on the measurement of the signal yields from the invariant mass distribution. These
 495 procedures use the distribution of $\cos(2\Delta\phi)$ versus invariant mass (where $\Delta\phi = \phi_D - \psi_2$) and the relation
 496 $v_2 = \langle \cos(2\Delta\phi) \rangle$. In the first procedure, the distribution of $\cos(2\Delta\phi)$ is considered for the signal region
 497 ($|M - m_D| < 3\sigma$) and the two side-band regions ($4 < |M - m_D| < 7\sigma$). The distribution of $\cos(2\Delta\phi)$
 498 for the background is obtained by averaging, bin-by-bin, the distributions of $\cos(2\Delta\phi)$ in the two side
 499 bands. This background distribution is then rescaled to the integral of the background fit function in the
 500 invariant mass signal region and it is subtracted from the total $\cos(2\Delta\phi)$ distribution in the signal region.
 501 In this way, the distribution of $\cos(2\Delta\phi)$ of the signal is obtained. Its mean value gives the D meson
 502 v_2 . In the second procedure, a distribution of $\langle \cos(2\Delta\phi) \rangle$ as a function of invariant mass is used for a
 503 simultaneous fit of the v_2 and the yield, as in the case of the two-particle correlation methods. These
 504 two alternative procedures result in D meson v_2 values that are consistent with those obtained from the
 505 event plane method with two $\Delta\phi$ bins. Therefore, no systematic uncertainty is taken for the v_2 extraction
 506 procedure.

507 The v_2 analysis was repeated with different sets of cuts for the selection of D meson candidates. A set
 508 of tighter and a set of looser cuts with respect to those described in Section 3.2 were considered for each
 509 D meson species, thus varying the signal yield by about 30–50% and, consequently, the significance
 510 and the signal-to-background ratio. The resulting v_2 values were found to be consistent within statistical
 511 uncertainties. Consequently, this contribution to the systematic uncertainty was neglected.

512 The uncertainty due to the event plane resolution was estimated with the two and three sub-event methods
 513 with an η gap. The three sub-events were defined using the TPC tracks and the signals in the two VZERO
 514 detectors. The resolutions estimated with these two methods differ by 6.9%, 2.0% and 2.3% in the 0–
 515 10%, 10–30% and 30–50% centrality classes, respectively (see right-hand panel of Fig. 1). A symmetric
 516 systematic uncertainty equal to the relative difference between R_2 values obtained with the two and three
 517 sub-event methods was assigned to the D meson v_2 .

518 The uncertainty due to the centrality dependence of the event plane resolution was estimated from the
 519 difference between two ways to define the average resolution in the centrality classes used in the analysis,
 520 starting from the resolutions in fine centrality intervals (see right-hand panel of Fig. 1). Namely, a
 521 plain arithmetic average and an average weighted with the D meson yield measured in smaller centrality
 522 classes (2.5% wide). The latter was estimated using D^0 meson raw yields in wide p_T intervals and the
 523 sum of the two $\Delta\phi$ intervals, in order to reduce the statistical fluctuations. The difference between these
 524 averages was found to be about 2%, 0.5% and 2% for the 0–10%, 10–30% and 30–50% centrality classes,
 525 respectively. The resulting total uncertainties on R_2 amount to 7%, 2% and 3% for the three centrality
 526 classes.

527 The distribution of collision impact parameters selected in a given centrality class slightly depends on the
 528 pseudo-rapidity coverage of the detector used for the centrality determination. The analysis was repeated
 529 using the number of tracks in the TPC as a centrality estimator, instead of the total signal measured in
 530 the VZERO detector. A relative systematic uncertainty of 10% was assigned to the v_2 values measured
 531 with the scalar product and two-particle cumulant methods, on the basis of the difference of the resulting
 532 v_2 values. This difference could originate from the dependence of the RFP multiplicity fluctuations on
 533 the centrality estimator. No significant difference was observed for the event plane method when using
 534 the TPC, instead of the VZERO, for the centrality determination.

535 The contribution of D mesons from B decays amounts to about 10–30% of the measured raw yield,
 536 depending on the D meson species and p_T . The systematic uncertainty associated with the assumption
 537 $v_2^{\text{feed-down}} = v_2^{\text{prompt}}$ was estimated by varying it in the interval $0 \leq v_2^{\text{feed-down}} \leq v_2^{\text{prompt}}$. This range covers
 538 all model predictions for v_2 of charm and beauty hadrons [19, 20, 42]. The central value of v_2^{prompt} was
 539 computed from Eq. (8) for the case $v_2^{\text{feed-down}} = v_2^{\text{prompt}}$, which results in $v_2^{\text{prompt}} = v_2^{\text{all}}$, independent of the
 540 value of f_{prompt} . A systematic uncertainty was assigned to cover the assumed range down to $v_2^{\text{feed-down}} = 0$,
 541 which yields $v_2^{\text{prompt}} = v_2^{\text{all}}/f_{\text{prompt}}$. For each meson species and in each p_T interval, a set of f_{prompt} values
 542 was computed by varying the heavy quark masses and the perturbative scales in the FONLL calculation
 543 as prescribed in [72], and the ratio $R_{AA}^{\text{feed-down}}/R_{AA}^{\text{prompt}}$ in the range $1 < R_{AA}^{\text{feed-down}}/R_{AA}^{\text{prompt}} < 3$. The smallest
 544 value of f_{prompt} was used to assign the uncertainty related to the B feed-down contribution to the elliptic
 545 flow of prompt D mesons. The maximum relative uncertainty is about ${}_{-0}^{+45}\%$.

546 4.2 Uncertainties on R_{AA}

547 For the analysis of the D^0 meson R_{AA} in-plane and out-of-plane, the same sources of systematic uncer-
 548 tainty as for the v_2 measurement with the event plane method were considered. Additional systematic
 549 uncertainties, which are specific to the R_{AA} measurement, stem from the tracking, selection and particle
 550 identification efficiencies, and from the uncertainty of the proton–proton reference yield. The evaluation
 551 of these uncertainties is similar as in [12] and it is described in the following.

552 In order to reduce the statistical fluctuations, the uncertainty of the D^0 yield extraction was estimated
 553 using the ϕ -integrated invariant mass distributions. The fit procedure was varied, as described for the v_2
 554 analysis. The resulting uncertainty is 7% for $2 < p_T < 8$ GeV/ c and 10% for $8 < p_T < 16$ GeV/ c . The
 555 systematic uncertainty on the correction factor for signal reflections, c_{refl} , was estimated by changing
 556 by $\pm 50\%$ the ratio of the integral of the reflections over the integral of the signal obtained from the
 557 simulation and used in the invariant mass fit with the reflections template. In addition, the shape of
 558 reflections invariant mass distribution template was varied using a polynomial parametrization of the
 559 distribution from the simulation, instead of a double-Gaussian parametrization. These variations resulted
 560 in an uncertainty of 1–2% for $2 < p_T < 4$ GeV/ c and of 5% for $4 < p_T < 16$ GeV/ c on the c_{refl} factor.

561 The systematic uncertainty of the tracking efficiency was estimated by comparing the probability to
 562 match the TPC tracks extrapolated to the ITS hits in data and simulation, and by varying the track quality
 563 selection criteria (for example, the minimum number of associated hits in the TPC and in the ITS and
 564 maximum χ^2/ndf of the momentum fit). The efficiency of the track matching and the association of hits in

565 the silicon pixel layers was found to be described by the simulation with maximal deviations on the level
 566 of 5% in the p_T range relevant for this analysis (0.5–15 GeV/ c). The effect of misassociating ITS hits to
 567 tracks was studied using simulations. It was found that the fraction of D mesons with at least one decay
 568 track with a wrong hit associated increases with centrality, due to the higher detector occupancy, and
 569 vanishes at high p_T , where the track extrapolation between ITS layers is more precise. In the centrality
 570 class 30–50%, this fraction is about 2% in the transverse momentum interval $2 < p_T < 16$ GeV/ c . It
 571 was verified that the signal selection efficiencies are the same for D mesons with and without wrong hit
 572 associations. The total systematic uncertainty of the track reconstruction procedure amounts to 5% for
 573 single tracks, which results in a 10% uncertainty for D^0 mesons (two-track final state).

574 The uncertainty of the correction for the selection on the decay topology was evaluated by repeating
 575 the analysis with different sets of cuts and was defined as the variation of the resulting corrected yields
 576 with respect to the value corresponding to the baseline cuts. This resulted in a variation up to 10% in
 577 the p_T intervals used in the analysis. The analysis was repeated without applying the PID selection and
 578 the resulting corrected yields were found to be consistent within 5% with those obtained with the PID
 579 selection. Therefore, a systematic uncertainty of 5% was assigned for the PID efficiency correction in
 580 the simulation.

581 The uncertainty of the efficiencies arising from the difference between the real and simulated D meson
 582 momentum distributions depends on the width of the p_T intervals and on the variation of the efficiencies
 583 within them. This uncertainty includes also the effect of the p_T dependence of the nuclear modification
 584 factor. The mean efficiency in a given p_T interval was computed by re-weighting the simulated D^0 meson
 585 yield according to the p_T distribution measured for D^0 mesons in central Pb–Pb collisions [12]. The
 586 systematic uncertainty was defined as the difference with respect to the efficiency computed using the
 587 p_T distribution from a FONLL calculation [72] multiplied by the R_{AA} value from one of the models [20]
 588 that closely describe the central value of the measurement (see Section 6). This uncertainty is of 2%
 589 in the interval $2 < p_T < 3$ GeV/ c , where the efficiency increases steeply with p_T , and below 1% for
 590 $p_T > 3$ GeV/ c .

591 The uncertainty of 3% on the event plane resolution correction factor R_2 in the 30–50% centrality class
 592 was propagated to the R_{AA} observables, resulting in an uncertainty in the range 0.5–2%, depending on
 593 the p_T interval.

594 The systematic uncertainty due to the subtraction of feed-down D mesons from B meson decays was
 595 estimated following the procedure described in [12]. The contribution of the uncertainties inherent in the
 596 FONLL perturbative calculation was included by varying the heavy-quark masses and the factorization
 597 and renormalization scales in the ranges proposed in [72]. This contribution partly cancels in the R_{AA}
 598 ratio, because these variations are done simultaneously for the Pb–Pb yield and for the pp reference
 599 cross section. The uncertainty introduced by the hypothesis on the value of the feed-down D meson R_{AA}
 600 was estimated from the variation $1 < R_{AA}^{\text{feed-down}}/R_{AA}^{\text{prompt}} < 3$. The total uncertainty due to the feed-down
 601 correction, which is common to the in-plane and out-of-plane R_{AA} , ranges between ${}_{-13}^{+9}\%$ at low p_T and
 602 ${}_{-12}^{+14}\%$ at high p_T . The hypothesis on the value of v_2 for D mesons from B decays, that was varied in the
 603 range $0 \leq v_2^{\text{feed-down}} \leq v_2^{\text{prompt}}$, introduces an additional contribution to the systematic uncertainty, which
 604 is anti-correlated between $R_{AA}^{\text{in-plane}}$ and $R_{AA}^{\text{out-of-plane}}$. This uncertainty is typically of ${}_{-0}^{+5}\%$ for in-plane and
 605 ${}_{-5}^{+0}\%$ for out-of-plane.

606 The uncertainty of the pp reference used for the calculation of R_{AA} has two contributions. The first is
 607 due to the systematic uncertainty of the measured D^0 meson p_T -differential yield at $\sqrt{s} = 7$ TeV and
 608 it is about 17%, approximately constant with p_T [55]. The second contribution is due to the scaling to
 609 $\sqrt{s} = 2.76$ TeV. It ranges from ${}_{-10}^{+31}\%$ at low p_T to about 5% at high p_T [12].

610 The uncertainties on the pp cross section normalization (3.5%) [55] and the average nuclear overlap

Table 3: Systematic uncertainties on the measurement of the D^0 meson R_{AA} in-plane and out-of-plane in the 30–50% centrality class for two p_T intervals. The uncertainties are grouped according to the type of correlation between the in-plane and out-of-plane cases.

p_T interval (GeV/c)	2–3	12–16
Uncorrelated uncertainties		
Yield extraction	7%	10%
Total uncorrelated	7%	10%
Correlated uncertainties		
Correction for reflections	1%	5%
Tracking efficiency	10%	10%
Cut efficiency	10%	10%
PID efficiency	5%	5%
D^0 p_T distribution in MC	2%	0
pp reference	$+20\%$ -35%	18%
Data syst.	17%	17%
\sqrt{s} scaling	$+10\%$ -31%	$+5\%$ -6%
B feed-down yield	$+9\%$ -13%	$+14\%$ -12%
Total correlated	$+22\%$ -37%	$+28\%$ -27%
Normalization uncertainties		
pp cross section norm.	3.5%	
$\langle T_{AA} \rangle$	4.7%	
Centrality class definition	2%	
Total normalization	6.2%	
Anti-correlated uncertainties		
Uncertainty on R_2	0.5%	0.5%
B feed-down v_2	in: $+4\%$; out: $+0\%$ out: -0% ; in: -6%	in: $+7\%$; out: $+0\%$ out: -5% ; in: -5%
Total anti-correlated	in: $+4\%$; out: $+0.5\%$ out: -0.5% ; in: -6%	in: $+7\%$; out: $+0.5\%$ out: -0.5% ; in: -5%

611 function $\langle T_{AA} \rangle$ (4.7% for the class 30–50%) were also included. The contribution due to the 1.1%
612 relative uncertainty on the fraction of the hadronic cross section used in the Glauber fit to determine the
613 centrality classes [53] was obtained by estimating the variation of the D meson dN/dp_T when the limits of
614 the centrality classes are shifted by $\pm 1.1\%$ (e.g. instead of 30–50%, 30.3–50.6% and 29.7–49.5%) [12].
615 The resulting uncertainty, common to all p_T intervals, is 2% for the 30–50% centrality class. The total
616 normalization uncertainty, computed taking the quadratic sum of these three contributions, is 6.2%.

617 The systematic uncertainties of R_{AA} were grouped in three categories, depending on their correlation be-
618 tween the in-plane and out-of-plane measurements. The uncorrelated systematic uncertainties affect the
619 two R_{AA} independently; this category includes only the yield extraction uncertainty. The correlated sys-
620 tematic uncertainties affect the two R_{AA} in the same way and do not affect their relative difference. The
621 uncertainties on the correction efficiencies (for track reconstruction, selection cuts, particle identification
622 and D^0 p_T distribution in the simulation) and on the correction for reflections, as well as those on the pp
623 reference, the variation of pQCD scales and the $R_{AA}^{\text{feed-down}}$ hypothesis used for the feed-down subtraction
624 are included in this category. Another correlated uncertainty is due to the normalization ($\langle T_{AA} \rangle$) and cen-
625 trality class definition), which is quoted separately. The anti-correlated systematic uncertainties could
626 shift the two R_{AA} in opposite directions, affecting their difference. This category includes the contri-
627 bution from the unknown azimuthal anisotropy of feed-down D mesons (variation of $v_2^{\text{feed-down}}$) and the
628 contribution from the event plane resolution correction factor. Within each category, the uncertainties
629 from different sources were added in quadrature.

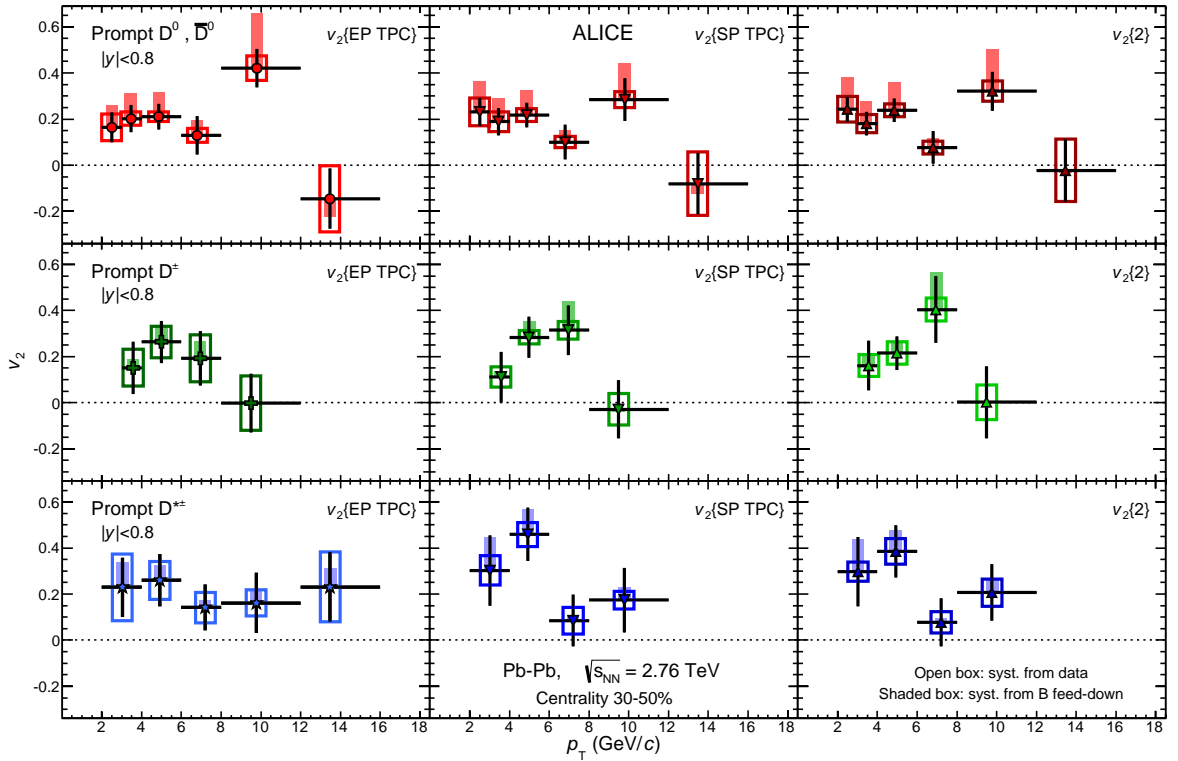


Figure 6: v_2 as a function of p_T in the 30–50% centrality class, for D^0 , D^+ and D^{*+} mesons (rows) with the event plane (from Ref. [46]), scalar product and two-particle cumulant methods (columns). For the first method, the event plane was estimated with TPC tracks in $0 < \eta < 0.8$; for the other methods, TPC tracks in $-0.8 < \eta < 0.8$ were used as RFP. The symbols are positioned at the average p_T measured within each interval.

630 5 Results

631 5.1 Elliptic flow

632 The elliptic flow v_2 measured with the event plane method is shown as a function of p_T in the left column
 633 of Fig. 6 for D^0 , D^+ and D^{*+} mesons in the 30–50% centrality class. The event plane was estimated
 634 from TPC tracks in the range $0 < \eta < 0.8$. The symbols are positioned horizontally at the average p_T of
 635 reconstructed D mesons. This value was determined as the average of the p_T distribution of candidates in
 636 the signal invariant mass region, after subtracting the contribution of the background candidates, which
 637 was estimated from the side bands. This average p_T of the reconstructed D mesons is larger than that of
 638 the produced D mesons, because the efficiency increases with increasing p_T (see Fig. 4). The vertical
 639 error bars represent the statistical uncertainty, the open boxes are the systematic uncertainties from the
 640 anisotropy determination and the event plane resolution, and the filled boxes are the uncertainties
 641 due to the B feed-down contribution. The elliptic flow of the three D meson species is consistent
 642 within statistical uncertainties and ranges between 0.1 and 0.3 in the interval $2 < p_T < 8$ GeV/c. For
 643 $p_T > 12$ GeV/c, v_2 is consistent with zero within the large statistical uncertainties. The central and
 644 right-most panels of the same figure show the v_2 results obtained with the scalar product and two-particle
 645 cumulant methods, respectively. The results from the three methods are consistent within statistical
 646 uncertainties for the three meson species.

647 Figure 7 shows the v_2 of the D^0 mesons measured with the event plane (left) and scalar product (right)
 648 methods using reference particles from the TPC detector (i.e. in a η range that overlaps with the D meson
 649 acceptance) or from the VZERO detectors at $-3.7 < \eta < -1.7$ and $2.8 < \eta < 5.1$ (i.e. with a large η

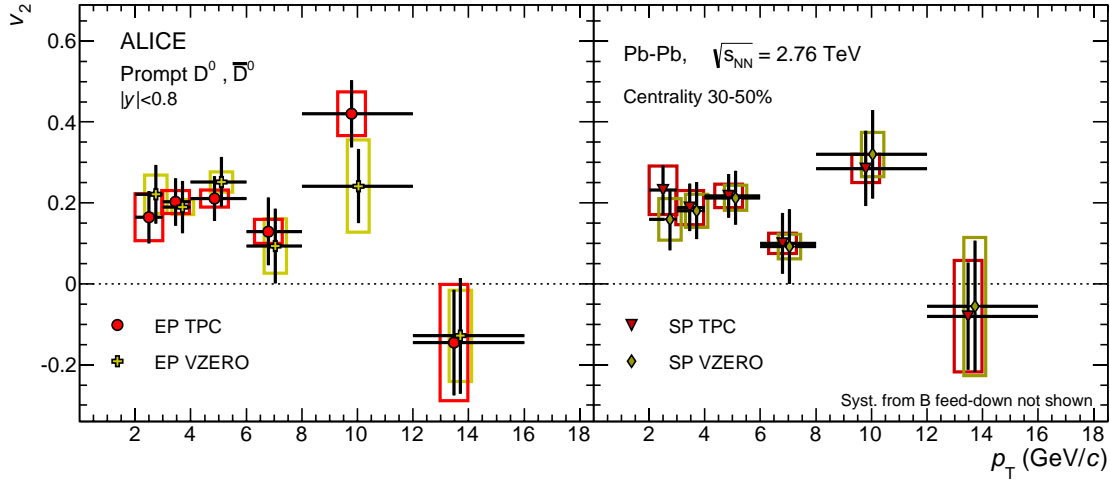


Figure 7: D^0 meson v_2 as a function of p_T in the 30–50% centrality class, with the reference particles from the TPC or from the VZERO detectors ($-3.7 < \eta < -1.7$ and $2.8 < \eta < 5.1$). Left: Event plane method. Right: Scalar product method. For visibility, the symbols for the VZERO case are slightly displaced horizontally.

650 gap with respect to the D mesons). The agreement between the results with and without η gap indicates
 651 that the bias due to non-flow correlations is within the statistical precision of the measurement.

652 For the 30–50% centrality class an average v_2 of D^0 , D^+ and D^{*+} was already computed in [46] from the
 653 event plane method results, using the statistical uncertainties as weights. The resulting D meson v_2 has
 654 a value 0.204 ± 0.030 (stat) ± 0.020 (syst) $^{+0.092}_{-0}$ (B feed-down), averaged over the p_T intervals 2–3, 3–4,
 655 4–6 GeV/c. This value is larger than zero with a significance, calculated from the combined statistical
 656 and systematic uncertainties, of 5.7σ .

657 Figure 8 shows the D^0 meson v_2 in the three centrality classes 0–10%, 10–30% and 30–50% as a function
 658 of p_T . The D^0 meson v_2 is compared with that of charged particles [35], for the same centrality classes. D
 659 meson and charged particle results are obtained with the event plane method using TPC and the VZERO
 660 detectors, respectively. The magnitude of v_2 is similar for charm hadrons and light-flavour hadrons,
 661 which dominate the charged-particle sample.

662 The centrality dependence of the D^0 elliptic flow is shown in Fig. 9 for three transverse momentum
 663 intervals in the range $2 < p_T < 6$ GeV/c. A decreasing trend of v_2 towards more central collisions is
 664 observed, as expected because of the decreasing initial geometrical anisotropy.

665 5.2 Nuclear modification factor in and out of the event plane

666 The nuclear modification factors of D^0 mesons in the 30–50% centrality class are shown in Fig. 10 for the
 667 in-plane and out-of-plane directions with respect to the event plane. The event plane was estimated with
 668 TPC tracks in $0 < \eta < 0.8$. The error bars represent the statistical uncertainties, which are to a large extent
 669 independent for the two azimuthal intervals, since they are dominated by the statistical uncertainties of
 670 the Pb–Pb data. The uncorrelated (empty boxes), correlated (brackets) and anti-correlated (shaded boxes)
 671 systematic uncertainties are shown separately. The normalization uncertainty, shown as a box at $R_{AA} = 1$,
 672 is common to both measurements.

673 A large suppression is observed in both directions with respect to the event plane for $p_T > 4$ GeV/c. At
 674 lower transverse momentum, the suppression appears to be reduced, especially in the in-plane direction,
 675 where R_{AA} reaches unity at a p_T of 2–3 GeV/c. Overall, a stronger suppression in the out-of-plane
 676 direction is observed. The ordering $R_{AA}^{\text{out-of-plane}} < R_{AA}^{\text{in-plane}}$ is equivalent to the observation of $v_2 > 0$ (as

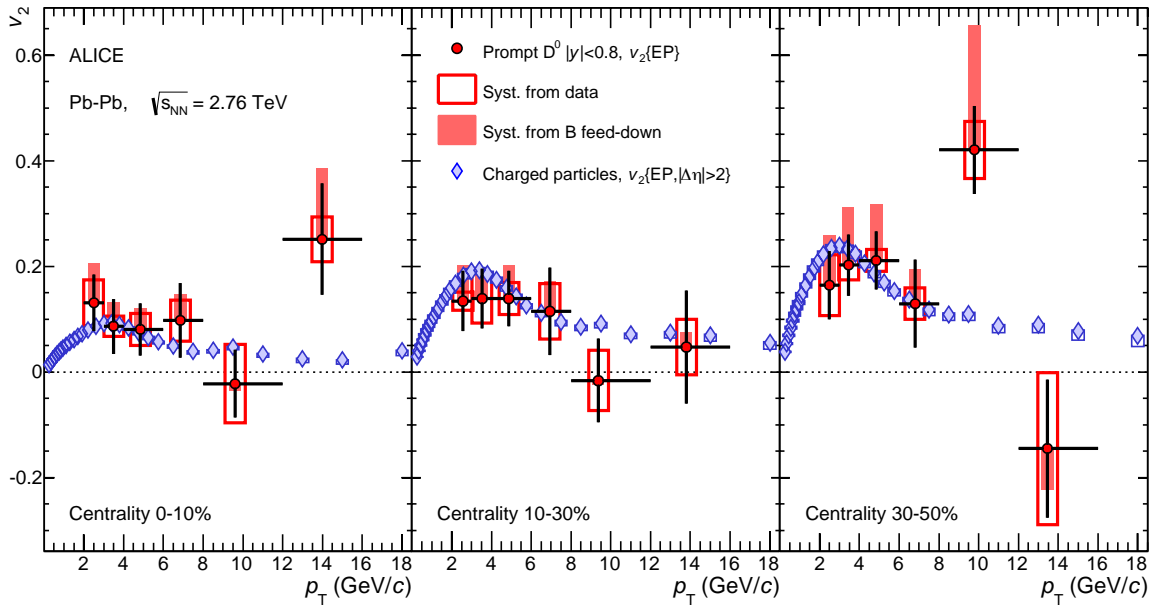


Figure 8: Comparison of prompt D^0 meson and charged-particle v_2 [35] in three centrality classes as a function of p_T . Both measurements are done with the event plane method. For charged particles a gap of two η units is used.

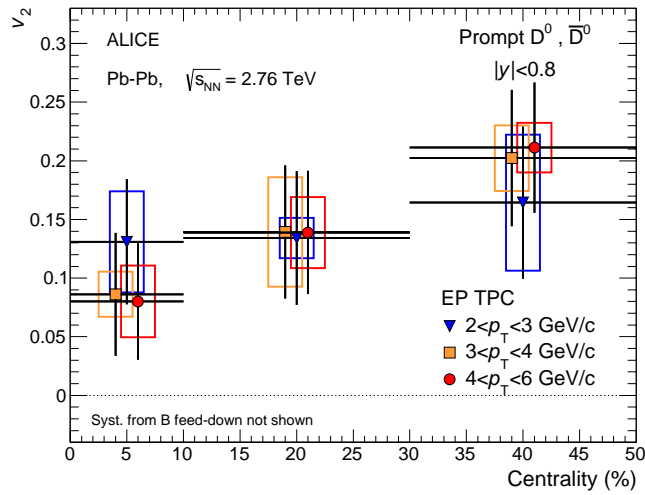


Figure 9: D^0 meson v_2 with event plane method in three p_T intervals as a function of centrality. For visibility, the points are displaced horizontally for two of the p_T intervals.

677 shown in the top-left panel of Fig. 6), since Eq. (4) can be expressed also as

$$v_2 = \frac{\pi R_{AA}^{\text{in-plane}} - R_{AA}^{\text{out-of-plane}}}{4 R_{AA}^{\text{in-plane}} + R_{AA}^{\text{out-of-plane}}} \quad (12)$$

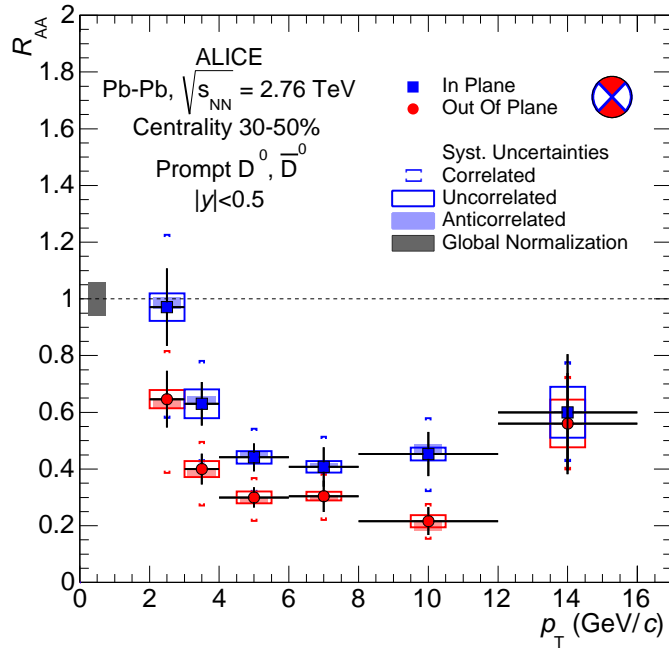


Figure 10: Nuclear modification factor R_{AA} of D^0 mesons in the 30–50% centrality class in two 90° -wide azimuthal intervals centred on the in-plane and on the out-of-plane directions. The correlated, uncorrelated, and anti-correlated contributions to the systematic uncertainty are shown separately.

6 Comparison with model calculations

A number of theoretical model calculations are available for the elliptic flow coefficient v_2 and the nuclear modification factor R_{AA} of heavy-flavour hadrons. Figure 11 shows a comprehensive comparison of these models to measurements of the R_{AA} of D^0 mesons in-plane and out-of-plane in the 30–50% centrality class, of the average R_{AA} of D^0 , D^+ and D^{*+} in the 0–20% centrality class [12], and of the v_2 averaged over the D meson species in the centrality class 30–50% [46].

The following models are considered and compared to data:

I WHDG [17]. This is a perturbative QCD calculation of parton energy loss, including both radiative (DGLV [77]) and collisional processes. A realistic collision geometry based on the Glauber model [9] is used, without hydrodynamical expansion, so that the anisotropy results only from path-length dependent energy loss. Hadronization is performed using vacuum fragmentation functions. The medium density is constrained on the basis of the π^0 R_{AA} in central collisions at $\sqrt{s_{NN}} = 200$ GeV and scaled to LHC energy according to the increase of the charged-particle multiplicity. The model describes well the D meson R_{AA} in the centrality interval 0–20% (slightly overestimating the suppression, as it does also for charged particles [12]), and gives an almost p_T -independent $v_2 \approx 0.06$, which is smaller than the measured values in the range $2 < p_T < 6$ GeV/c. Consequently, the difference between the in-plane and out-of-plane R_{AA} suppression is underestimated: the model describes well the out-of-plane R_{AA} and lies below the in-plane R_{AA} .

II MC@sHQ+EPOS, Coll+Rad(LPM) [78]. This pQCD model includes collisional and radiative (with Landau-Pomeranchuk-Migdal correction [79]) energy loss mechanisms for heavy quarks with running strong coupling constant. The cross sections of the interaction processes are increased by a correction factor tuned to describe the heavy-flavour decay electron R_{AA} at RHIC; the same factor is used at LHC energies. The medium fluid dynamical expansion is based on the EPOS

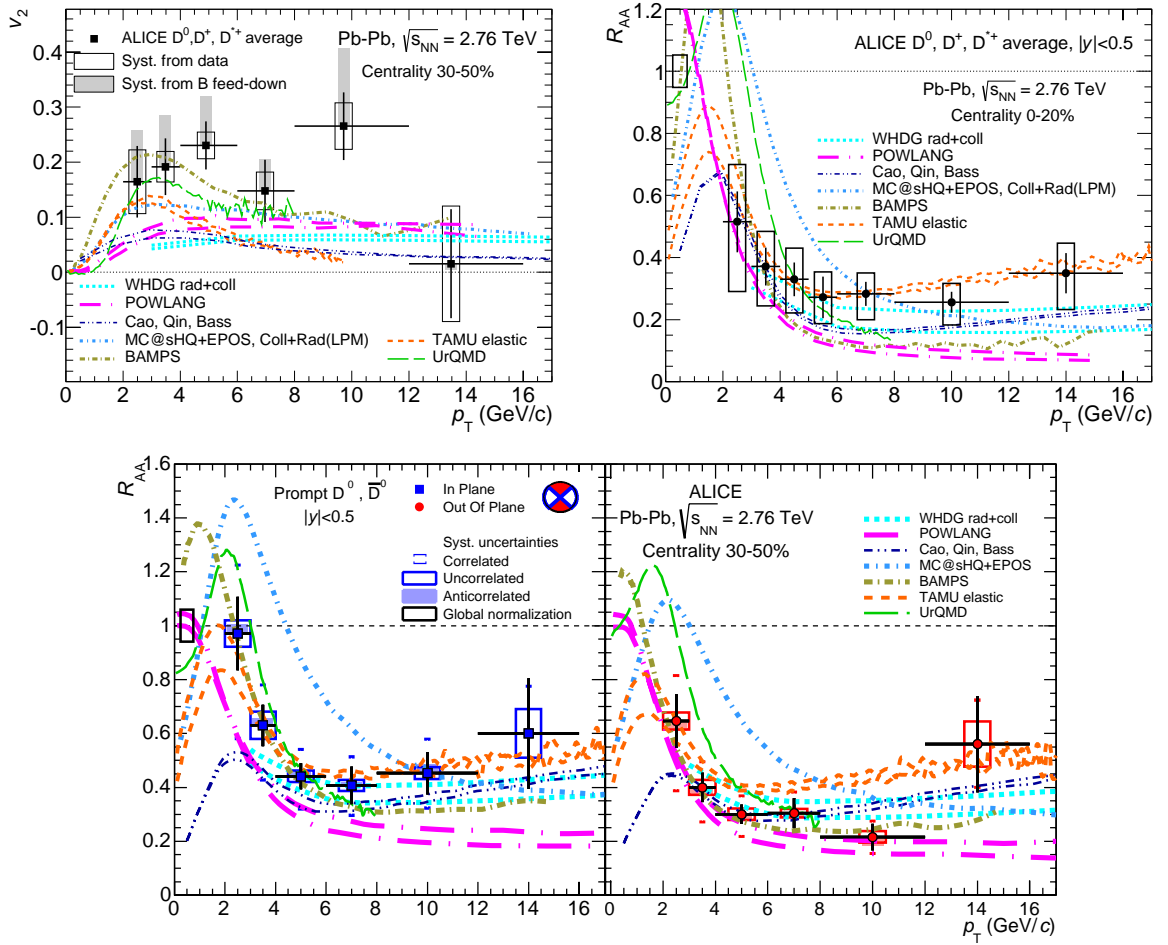


Figure 11: (colour online) Model comparisons for average D meson v_2 in the 30–50% centrality class (upper-left), average D meson R_{AA} in the 0–20% centrality class (upper-right) [12], D^0 R_{AA} in-plane and out-of-plane in the 30–50% centrality class (lower panels). The seven model calculations are described in the text: WHDG rad+coll [17], POWLANG [18], Cao, Qin, Bass [45], MC@sHQ+EPOS, Coll+Rad(LPM) [78], BAMPS [20], TAMU elastic [43], UrQMD [44]. The models WHDG rad+coll, POWLANG, TAMU elastic and UrQMD are shown by two lines that represent their uncertainty.

701 model [80]. A component of recombination of heavy quarks with light-flavour quarks from the
 702 QGP is also incorporated in the model. This model yields a substantial anisotropy ($v_2 \approx 0.12$ – 0.08
 703 from low to high p_T), which is close to that observed in data. The nuclear modification factor is
 704 substantially overestimated below $p_T \approx 5$ GeV/ c and correctly described at higher p_T .

705 III TAMU elastic [43]. This is a heavy-flavour transport model based on collisional, elastic processes
 706 only. The heavy-quark transport coefficient is calculated within a non-perturbative T -matrix ap-
 707 proach, where the interactions proceed via resonance formation that transfers momentum from the
 708 heavy quarks to the medium constituents. The model includes hydrodynamic medium evolution,
 709 constrained by light-flavour hadron spectra and elliptic flow data, and a component of recombi-
 710 nation of heavy quarks with light-flavour quarks from the QGP. Diffusion of heavy-flavour hadrons
 711 in the hadronic phase is also included. The model provides a good description of the observed
 712 suppression of D mesons over the entire p_T range. The maximum anisotropy, v_2 of about 0.13 at
 713 $2 < p_T < 4$ GeV/ c , is close to that observed in the data. Towards larger p_T , the model tends to
 714 underestimate v_2 , as well as the difference of the in-plane and out-of-plane R_{AA} .

- 715 IV POWLANG [18]. This transport model is based on collisional processes treated within the frame-
716 work of Langevin dynamics, within an expanding deconfined medium described by relativistic
717 viscous hydrodynamics. The transport coefficients entering into the relativistic Langevin equation
718 are evaluated by matching the hard-thermal-loop calculation of soft collisions with a perturbative
719 QCD calculation for hard scatterings. Hadronization is implemented via vacuum fragmentation
720 functions. This model overestimates the high- p_T suppression, it yields a value for v_2 significantly
721 smaller than observed in data and also underestimates the difference between the in-plane and
722 out-of-plane suppression.
- 723 V BAMPS [20]. This partonic transport model is based on the Boltzmann approach to multi-
724 parton scattering. Heavy quarks interact with the medium via collisional processes computed
725 with running strong coupling constant. Hadronization is performed using vacuum fragmentation
726 functions. The lack of radiative processes is accounted for by scaling the binary cross section
727 with a correction factor, which is tuned to describe the heavy-flavour decay electron elliptic flow
728 and nuclear modification factor at RHIC. When applied to calculations for LHC energy, this
729 correction factor results in an underestimation of the D meson R_{AA} for $p_T > 5$ GeV/ c and a large
730 azimuthal anisotropy, with v_2 values up to 0.20, similar to those observed in the data. The nuclear
731 modification factors in-plane and out-of-plane are well described up to 5 GeV/ c , while for higher
732 p_T the in-plane R_{AA} is underestimated.
- 733 VI UrQMD [44]. The Langevin approach for the transport of heavy quarks is in this case implemented
734 within the UrQMD model [81]. This model includes a realistic description of the medium evolution
735 by combining hadronic transport and ideal hydrodynamics. The transport of heavy quarks is cal-
736 culated on the basis of a resonance model with a decoupling temperature of 130 MeV. Hadroniza-
737 tion via quark coalescence is included. The calculation parameters are tuned to reproduce the
738 heavy-flavour measurements at RHIC ($\sqrt{s_{NN}} = 200$ GeV) and kept unchanged for calculations at
739 the LHC energy. The model describes the measured D meson v_2 , as well as R_{AA} in the interval
740 $4 < p_T < 8$ GeV/ c , but it fails to reproduce the significant suppression measured for R_{AA} at p_T of
741 $2-3$ GeV/ c .
- 742 VII Cao, Qin, Bass [45]. This model is also based on the Langevin approach. In addition to quasi-
743 elastic scatterings, radiative energy loss is incorporated by treating gluon radiation as an additional
744 force term. The space-time evolution of the medium is modelled using a viscous hydrodynamic
745 simulation. The hadronization of heavy quarks has a contribution based on the recombination
746 mechanism. With respect to [45], the curves shown in the figure were obtained with a more
747 recent parametrization for the nuclear shadowing of the parton distribution functions. This model
748 provides a good description of the R_{AA} data in central collisions, but it yields a value of v_2
749 significantly smaller than the measured one (similarly to the WHDG and POWLANG models)
750 and also underestimates the difference between the in-plane and out-of-plane suppression.
- 751 Overall, the anisotropy is qualitatively described by the models that include both charm quark energy loss
752 in a geometrically anisotropic medium and mechanisms that transfer to charm quarks the elliptic flow in-
753 duced during the system expansion. These mechanisms include collisional processes (MC@sHQ+EPOS,
754 Coll+Rad(LPM) [78], BAMPS [20]) and resonance scattering with hadronization via recombination
755 (TAMU elastic [43], UrQMD [44]) in a hydrodynamically expanding QGP. Models that do not include
756 a collective expansion of the medium or lack a contribution to the hadronization of charm quarks from
757 recombination with light quarks from the medium predict in general a smaller anisotropy than observed
758 in the data. The comparison for R_{AA} and v_2 shows that it is challenging to simultaneously describe the
759 large suppression of D mesons in central collisions and their anisotropy in non-central collisions. In gen-
760 eral, the models that are best in describing R_{AA} tend to underestimate v_2 and the models that describe v_2
761 tend to underestimate the measured R_{AA} at high p_T . It is also worth noting that most of the calculations
762 do reproduce the RHIC measurements of heavy-flavour decay electron R_{AA} and v_2 .

7 Summary

We have presented a comprehensive set of results on the azimuthal anisotropy of charm production at central rapidity in Pb–Pb collisions at $\sqrt{s_{NN}} = 2.76$ TeV, obtained by reconstructing the decays $D^0 \rightarrow K^- \pi^+$, $D^+ \rightarrow K^- \pi^+ \pi^+$ and $D^{*+} \rightarrow D^0 \pi^+$.

The azimuthal anisotropy parameter v_2 was measured with the event plane, scalar product and two-particle cumulant methods, as a function of transverse momentum for semi-central collisions in the 30–50% quantile of the hadronic cross section. The measured anisotropy was found to be consistent among D meson species, as well as for the three methods. The average v_2 of the three mesons in the interval $2 < p_T < 6$ GeV/ c is larger than zero with a significance of 5.7σ , combining statistical and systematic uncertainties. With a smaller significance, a positive v_2 is also observed for $p_T > 6$ GeV/ c , likely to originate from a path-length dependence of the partonic energy loss. The azimuthal anisotropy of D^0 mesons, which have larger statistical significance than D^+ and D^{*+} , was also measured in the centrality classes 0–10% and 10–30%. For all three centrality classes, the D^0 meson v_2 is comparable in magnitude to that of inclusive charged particles. An indication for a decrease of v_2 towards more central collisions was observed for $3 < p_T < 6$ GeV/ c .

The anisotropy was also quantified in terms of the D^0 meson nuclear modification factor R_{AA} , measured in the direction of the event plane and orthogonal to it. For $p_T > 3$ GeV/ c , a stronger suppression relative to proton–proton collisions is observed in the out-of-plane direction, where the average path length of heavy quarks through the medium is larger.

The results indicate that the interactions with medium constituents transfer to charm quarks information on the azimuthal anisotropy of the system during its collective expansion.

The new results for v_2 and R_{AA} measured in and out of the event plane, as well as previously published R_{AA} in the most central collisions [12], were compared with model calculations. The anisotropy is best described by the models that include mechanisms, like collisional energy loss, that transfer to charm quarks the elliptic flow induced during the system expansion. In some of these models the charm meson v_2 is further enhanced by charm quark recombination with light quarks from the medium. However, it is challenging for models to describe simultaneously the large suppression of D mesons in central collisions and their anisotropy in non-central collisions. The results reported in this article provide important constraints on the mechanisms of heavy-quark energy loss and on the transport properties of the expanding medium produced in high-energy heavy-ion collisions.

Acknowledgements

The ALICE Collaboration would like to thank all its engineers and technicians for their invaluable contributions to the construction of the experiment and the CERN accelerator teams for the outstanding performance of the LHC complex. The ALICE Collaboration gratefully acknowledges the resources and support provided by all Grid centres and the Worldwide LHC Computing Grid (WLCG) collaboration. The ALICE Collaboration acknowledges the following funding agencies for their support in building and running the ALICE detector: State Committee of Science, World Federation of Scientists (WFS) and Swiss Fonds Kidagan, Armenia, Conselho Nacional de Desenvolvimento Científico e Tecnológico (CNPq), Financiadora de Estudos e Projetos (FINEP), Fundação de Amparo à Pesquisa do Estado de São Paulo (FAPESP); National Natural Science Foundation of China (NSFC), the Chinese Ministry of Education (CMOE) and the Ministry of Science and Technology of China (MSTC); Ministry of Education and Youth of the Czech Republic; Danish Natural Science Research Council, the Carlsberg Foundation and the Danish National Research Foundation; The European Research Council under the European Community’s Seventh Framework Programme; Helsinki Institute of Physics and the Academy of Finland; French CNRS-IN2P3, the ‘Region Pays de Loire’, ‘Region Alsace’, ‘Region Auvergne’ and

808 CEA, France; German BMBF and the Helmholtz Association; General Secretariat for Research and
809 Technology, Ministry of Development, Greece; Hungarian OTKA and National Office for Research and
810 Technology (NKTH); Department of Atomic Energy and Department of Science and Technology of the
811 Government of India; Istituto Nazionale di Fisica Nucleare (INFN) and Centro Fermi - Museo Storico
812 della Fisica e Centro Studi e Ricerche "Enrico Fermi", Italy; MEXT Grant-in-Aid for Specially Pro-
813 moted Research, Japan; Joint Institute for Nuclear Research, Dubna; National Research Foundation of
814 Korea (NRF); CONACYT, DGAPA, México, ALFA-EC and the EPLANET Program (European Particle
815 Physics Latin American Network); Stichting voor Fundamenteel Onderzoek der Materie (FOM) and
816 the Nederlandse Organisatie voor Wetenschappelijk Onderzoek (NWO), Netherlands; Research Council
817 of Norway (NFR); Polish Ministry of Science and Higher Education; National Science Centre, Poland;
818 Ministry of National Education/Institute for Atomic Physics and CNCS-UEFISCDI - Romania; Min-
819 istry of Education and Science of Russian Federation, Russian Academy of Sciences, Russian Federal
820 Agency of Atomic Energy, Russian Federal Agency for Science and Innovations and The Russian Found-
821 ation for Basic Research; Ministry of Education of Slovakia; Department of Science and Technology,
822 South Africa; CIEMAT, EELA, Ministerio de Economía y Competitividad (MINECO) of Spain, Xunta
823 de Galicia (Consellería de Educación), CEADEN, Cubaenergía, Cuba, and IAEA (International Atomic
824 Energy Agency); Swedish Research Council (VR) and Knut & Alice Wallenberg Foundation (KAW);
825 Ukraine Ministry of Education and Science; United Kingdom Science and Technology Facilities Coun-
826 cil (STFC); The United States Department of Energy, the United States National Science Foundation,
827 the State of Texas, and the State of Ohio.

828 References

- 829 [1] F. Karsch, J. Phys. Conf. Ser. **46** (2006) 122.
830 [2] S. Borsanyi *et al.* [Wuppertal-Budapest Collaboration], JHEP **1009** (2010) 073;
831 S. Borsanyi, G. Endrodi, Z. Fodor, A. Jakovac, S. D. Katz, S. Krieg, C. Ratti and K. K. Szabo,
832 JHEP **1011** (2010) 077.
833 [3] A. Bazavov *et al.*, Phys. Rev. D **85** (2012) 054503.
834 [4] P. Petreczky, PoS ConfinementX2012 (2012) 028, arXiv:1301.6188 [hep-lat].
835 [5] P. Braun-Munzinger, J. Phys. G **34** (2007) S471.
836 [6] M. Gyulassy and M. Plumer, Phys. Lett. B **243** (1990) 432.
837 [7] R. Baier, Y. L. Dokshitzer, A. H. Mueller, S. Peigne and D. Schiff, Nucl. Phys. B **484** (1997) 265.
838 [8] M. H. Thoma and M. Gyulassy, Nucl. Phys. B **351** (1991) 491;
839 E. Braaten and M. H. Thoma, Phys. Rev. D **44** (1991) 1298; Phys. Rev. D **44** (1991) 2625.
840 [9] R. J. Glauber in Lectures in Theoretical Physics, NY, 1959, Vol. 1, 315;
841 M. Miller *et al.*, Ann. Rev. Nucl. Part. Sci. **57** (2007) 205.
842 [10] S. S. Adler *et al.* [PHENIX Collaboration], Phys. Rev. Lett. **96** (2006) 032301;
843 A. Adare *et al.* [PHENIX Collaboration], Phys. Rev. C **84** (2011) 044905.
844 [11] B. I. Abelev *et al.* [STAR Collaboration] Phys. Rev. Lett. **98** (2007) 192301.
845 [12] B. Abelev *et al.* [ALICE Collaboration], JHEP **1209** (2012) 112.
846 [13] B. Abelev *et al.* [ALICE Collaboration], Phys. Rev. Lett. **109** (2012) 112301.
847 [14] S. Chatrchyan *et al.* [CMS Collaboration], JHEP **1205** (2012) 063.
848 [15] N. Armesto, A. Dainese, C. A. Salgado and U. A. Wiedemann, Phys. Rev. D **71** (2005) 054027.
849 [16] Y. He, I. Vitev and B. -W. Zhang, Phys. Lett. B **713** (2012) 224.
850 [17] S. Wicks, W. A. Horowitz, M. Djordjevic, and M. Gyulassy, Nucl. Phys. A **784** (2007) 426;
851 W. A. Horowitz and M. Gyulassy, Nucl. Phys. A **872** (2011) 265;

- 852 W. A. Horowitz, AIP Conf. Proc. **1441** (2012) 889.
- 853 [18] W. M. Alberico *et al.*, Eur. Phys. J. C **71** (2011) 1666; J. Phys. G **38** (2011) 124144.
- 854 [19] P. B. Gossiaux, R. Bierkandt and J. Aichelin, Phys. Rev. C **79** (2009) 044906.
- 855 P. B. Gossiaux, J. Aichelin, T. Gousset and V. Guiho, J. Phys. G **37** (2010) 094019.
- 856 [20] O. Fochler, J. Uphoff, Z. Xu and C. Greiner, Phys. Rev. C **84** (2011) 024908; J. Phys. G **38** (2011)
- 857 124152; Phys. Lett. B **717** (2012) 430.
- 858 [21] A. Buzzatti and M. Gyulassy, Phys. Rev. Lett. **108** (2012) 022301.
- 859 [22] S. Batsouli, S. Kelly, M. Gyulassy and J. L. Nagle, Phys. Lett. B **557** (2003) 26.
- 860 [23] V. Greco, C. M. Ko and R. Rapp, Phys. Lett. B **595** (2004) 202.
- 861 [24] A. Andronic, P. Braun-Munzinger, K. Redlich and J. Stachel, Phys. Lett. B **571** (2003) 36.
- 862 [25] E. Abbas *et al.* [ALICE Collaboration], Phys. Rev. Lett. **111** (2013) 162301.
- 863 [26] Y. Liu, N. Xu and P. Zhuang, Nucl. Phys. A **834** (2010) 317c.
- 864 [27] X. Zhao, A. Emerick and R. Rapp, Nucl. Phys. A **904-905** (2013) 611c.
- 865 [28] M. Gyulassy, I. Vitev and X. N. Wang, Phys. Rev. Lett. **86** (2001) 2537.
- 866 [29] E. V. Shuryak, Phys. Rev. C **66** (2002) 027902.
- 867 [30] J. Y. Ollitrault, Phys. Rev. D **46** (1992) 229.
- 868 [31] P. F. Kolb, U. W. Heinz in Hwa, R.C. (ed.) *et al.*: Quark gluon plasma, 634-714 [nucl-th/0305084].
- 869 [32] J. Adams *et al.* [STAR Collaboration], Phys. Rev. C **72** (2005) 014904.
- 870 [33] S. Afanasiev *et al.* [PHENIX Collaboration], Phys. Rev. C **80** (2009) 054907.
- 871 [34] K. Aamodt *et al.* [ALICE Collaboration], Phys. Rev. Lett. **105** (2010) 252302.
- 872 [35] B. Abelev *et al.* [ALICE Collaboration], Phys. Lett. B **719** (2013) 18.
- 873 [36] G. Aad *et al.* [ATLAS Collaboration], Phys. Rev. C **86** (2012) 014907.
- 874 [37] S. Chatrchyan *et al.* [CMS Collaboration], Phys. Rev. C **87** (2013) 014902.
- 875 [38] M. Luzum and P. Romatschke, Phys. Rev. Lett. **103** (2009) 262302.
- 876 [39] A. Adare *et al.* [PHENIX Collaboration], Phys. Rev. C **84** (2011) 044905.
- 877 [40] G. D. Moore and D. Teaney, Phys. Rev. C **71** (2005) 064904.
- 878 [41] H. van Hees, V. Greco, and R. Rapp, Phys. Rev. C **73** (2006) 034913;
- 879 H. van Hees, M. Mannarelli, V. Greco, and R. Rapp, Phys. Rev. Lett. **100** (2008) 192301.
- 880 [42] M. He, R. J. Fries and R. Rapp, Phys. Rev. C **86** (2012) 014903.
- 881 [43] M. He, R. J. Fries and R. Rapp, arXiv:1401.3817 [nucl-th] (2014).
- 882 [44] T. Lang, H. van Hees, J. Steinheimer and M. Bleicher, arXiv:1211.6912 [hep-ph];
- 883 T. Lang, H. van Hees, J. Steinheimer, Y. -P. Yan and M. Bleicher, J. Phys. Conf. Ser. **426** (2013)
- 884 012032.
- 885 [45] S. Cao, G. -Y. Qin and S. A. Bass, Phys. Rev. C **88** (2013) 044907.
- 886 [46] B. Abelev *et al.* [ALICE Collaboration], Phys. Rev. Lett. **111** (2013) 102301.
- 887 [47] K. Aamodt *et al.* [ALICE Collaboration], JINST **3** (2008) S08002.
- 888 [48] K. Aamodt *et al.* [ALICE Collaboration], JINST **5** (2010) P03003.
- 889 [49] A. Rossi [for the ALICE Collaboration], PoS(Vertex2010)017, arXiv:1101.3491 (2011).
- 890 [50] J. Alme *et al.*, Nucl. Instrum. Meth. A **622** (2010) 316.
- 891 [51] A. Akindinov *et al.*, Eur. Phys. J. Plus **128** (2013) 44.
- 892 [52] E. Abbas *et al.* [ALICE Collaboration], JINST **8** (2013) P10016.
- 893 [53] B. Abelev *et al.* [ALICE Collaboration], Phys. Rev. C **88** (2013) 044909.
- 894 [54] J. Beringer *et al.* [Particle Data Group], Phys. Rev. D **86** (2012) 010001.
- 895 [55] B. Abelev *et al.* [ALICE Collaboration], JHEP **1201** (2012) 128.

- 896 [56] B. Abelev *et al.* [ALICE Collaboration], JHEP **1207** (2012) 191.
- 897 [57] A. M. Poskanzer and S. A. Voloshin, Phys. Rev. C **58** (1998) 1671.
- 898 [58] C. Adler *et al.* [STAR Collaboration], Phys. Rev. C **66** (2002) 034904.
- 899 [59] A. Bilandzic, R. Snellings and S. Voloshin, Phys. Rev. C **83** (2011) 044913.
- 900 [60] I. Selyuzhenkov and S. Voloshin, Phys. Rev. C **77** (2008) 034904.
- 901 [61] M. Luzum and J.-Y. Ollitrault, Phys. Rev. C **87** (2013) 044907.
- 902 [62] K. Aamodt *et al.* [ALICE Collaboration], Phys. Lett. B **708** (2012) 249.
- 903 [63] G. Aad *et al.* [ATLAS Collaboration], Phys. Rev. C **86** (2012) 014907.
- 904 [64] K. Aamodt *et al.*, [ALICE Collaboration], Phys. Rev. Lett. **105** (2010) 252302.
- 905 [65] K. Aamodt *et al.*, [ALICE Collaboration], Phys. Rev. Lett. **107** (2011) 032301.
- 906 [66] A. Bilandzic, CERN-THESIS-2012-018 (2012).
- 907 [67] N. Borghini, P.M. Dinh, J.-Y. Ollitrault, arXiv:nucl-ex/0110016 (2001).
- 908 [68] T. Sjöstrand, S. Mrenna, P. Skands, JHEP **05** (2006) 026.
- 909 [69] X.-N. Wang and M. Gyulassy, Phys. Rev. D **44** (1991) 3501.
- 910 [70] R. Brun *et al.*, CERN Program Library Long Write-up, W5013, GEANT Detector Description and
911 Simulation Tool (1994).
- 912 [71] P. Z. Skands, arXiv:0905.3418 [hep-ph] (2009).
- 913 [72] M. Cacciari, S. Frixione, N. Houdeau, M. L. Mangano, P. Nason and G. Ridolfi, JHEP **1210** (2012)
914 137.
- 915 [73] D. J. Lange, Nucl. Instrum. Methods A **462** (2001) 152.
- 916 [74] A. Grelli [for the ALICE Collaboration], arXiv:1310.7366 [hep-ex].
- 917 [75] CMS Collaboration, CMS-PAS-HIN-12-014 (2012).
- 918 [76] R. Averbek, N. Bastid, Z. C. del Valle, P. Crochet, A. Dainese and X. Zhang, arXiv:1107.3243
919 [hep-ph].
- 920 [77] M. Djordjevic and M. Gyulassy, Nucl. Phys. A **733** (2004) 265.
- 921 [78] M. Nahrgang, J. Aichelin, P. B. Gossiaux and K. Werner, Phys. Rev. C **89** (2014) 014905.
- 922 [79] R. Baier, D. Schiff, and B. G. Zakharov, Ann. Rev. Nucl. Part. Sci. **50** (2000) 37.
- 923 [80] K. Werner, I. Karpenko, T. Pierog, M. Bleicher and K. Mikhailov, Phys. Rev. C **82** (2010) 044904;
924 K. Werner, I. Karpenko, M. Bleicher, T. Pierog and S. Porteboeuf-Houssais, Phys. Rev. C **85** (2012)
925 064907.
- 926 [81] S. A. Bass *et al.*, Prog. Part. Nucl. Phys. **41** (1998) 255;
927 M. Bleicher *et al.*, J. Phys. G **25** (1999) 1859.

928 **A The ALICE Collaboration**

- 929 B. Abelev⁶⁹, J. Adam³⁷, D. Adamová⁷⁷, M.M. Aggarwal⁸¹, M. Agnello^{105,88}, A. Agostinelli²⁶, N. Agrawal⁴⁴,
930 Z. Ahammed¹²⁴, N. Ahmad¹⁸, I. Ahmed¹⁵, S.U. Ahn⁶², S.A. Ahn⁶², I. Aimo^{105,88}, S. Aiola¹²⁹, M. Ajaz¹⁵,
931 A. Akindinov⁵³, S.N. Alam¹²⁴, D. Aleksandrov⁹⁴, B. Alessandro¹⁰⁵, D. Alexandre⁹⁶, A. Alici^{12,99}, A. Alkin³,
932 J. Alme³⁵, T. Alt³⁹, S. Altinpinar¹⁷, I. Altsybeev¹²³, C. Alves Garcia Prado¹¹³, C. Andrei^{72,72}, A. Andronic⁹¹,
933 V. Anguelov⁸⁷, J. Anielski⁴⁹, T. Antičić⁹², F. Antinori¹⁰², P. Antonioli⁹⁹, L. Aphecetche¹⁰⁷,
934 H. Appelshäuser⁴⁸, S. Arcelli²⁶, N. Armesto¹⁶, R. Arnaldi¹⁰⁵, T. Aronsson¹²⁹, I.C. Arsene⁹¹, M. Arslandok⁴⁸,
935 A. Augustinus³⁴, R. Averbeck⁹¹, T.C. Awes⁷⁸, M.D. Azmi⁸³, M. Bach³⁹, A. Badalà¹⁰¹, Y.W. Baek^{64,40},
936 S. Bagnasco¹⁰⁵, R. Bailhache⁴⁸, R. Bala⁸⁴, A. Baldisseri¹⁴, F. Baltasar Dos Santos Pedrosa³⁴, R.C. Baral⁵⁶,
937 R. Barbera²⁷, F. Barile³¹, G.G. Barnaföldi¹²⁸, L.S. Barnby⁹⁶, V. Barret⁶⁴, J. Bartke¹¹⁰, M. Basile²⁶,
938 N. Bastid⁶⁴, S. Basu¹²⁴, B. Bathen⁴⁹, G. Batigne¹⁰⁷, A. Batista Camejo⁶⁴, B. Batyunya⁶¹, P.C. Batzing²¹,
939 C. Baumann⁴⁸, I.G. Bearden⁷⁴, H. Beck⁴⁸, C. Bedda⁸⁸, N.K. Behera⁴⁴, I. Belikov⁵⁰, F. Bellini²⁶,
940 R. Bellwied¹¹⁵, E. Belmont-Moreno⁵⁹, R. Belmont III¹²⁷, V. Belyaev⁷⁰, G. Bencedi¹²⁸, S. Beole²⁵,
941 I. Berceanu⁷², A. Bercuci⁷², Y. Berdnikov^{ii,79}, D. Berenyi¹²⁸, M.E. Berger⁸⁶, R.A. Bertens⁵², D. Berzano²⁵,
942 L. Betev³⁴, A. Bhasin⁸⁴, I.R. Bhat⁸⁴, A.K. Bhati⁸¹, B. Bhattacharjee⁴¹, J. Bhom¹²⁰, L. Bianchi²⁵,
943 N. Bianchi⁶⁶, C. Bianchin⁵², J. Bielčik³⁷, J. Bielčíková⁷⁷, A. Bilandzic⁷⁴, S. Bjelogrić⁵², F. Blanco¹⁰,
944 D. Blau⁹⁴, C. Blume⁴⁸, F. Bock^{87,68}, A. Bogdanov⁷⁰, H. Bøggild⁷⁴, M. Bogolyubsky¹⁰⁶, F.V. Böhmer⁸⁶,
945 L. Boldizsár¹²⁸, M. Bombara³⁸, J. Book⁴⁸, H. Borel¹⁴, A. Borissov^{90,127}, F. Bossú⁶⁰, M. Botje⁷⁵, E. Botta²⁵,
946 S. Böttger^{47,47}, P. Braun-Munzinger⁹¹, M. Bregant¹¹³, T. Breitner⁴⁷, T.A. Broker⁴⁸, T.A. Browning⁸⁹,
947 M. Broz³⁷, E. Bruna¹⁰⁵, G.E. Bruno³¹, D. Budnikov⁹³, H. Buesching⁴⁸, S. Bufalino¹⁰⁵, P. Buncic³⁴,
948 O. Busch⁸⁷, Z. Buthelezi⁶⁰, D. Caffarri²⁸, X. Cai⁷, H. Caines¹²⁹, L. Calero Diaz⁶⁶, A. Caliva⁵²,
949 E. Calvo Villar⁹⁷, P. Camerini²⁴, F. Carena³⁴, W. Carena³⁴, J. Castillo Castellanos¹⁴, E.A.R. Casula²³,
950 V. Catanescu⁷², C. Cavicchioli³⁴, C. Ceballos Sanchez⁹, J. Cepila³⁷, P. Cerello¹⁰⁵, B. Chang¹¹⁶,
951 S. Chapeland³⁴, J.L. Charvet¹⁴, S. Chattopadhyay¹²⁴, S. Chattopadhyay⁹⁵, V. Chelnokov³, M. Cherney⁸⁰,
952 C. Cheshkov¹²², B. Cheynis¹²², V. Chibante Barroso³⁴, D.D. Chinellato¹¹⁵, P. Chochula³⁴, M. Chojnacki⁷⁴,
953 S. Choudhury¹²⁴, P. Christakoglou⁷⁵, C.H. Christensen⁷⁴, P. Christiansen³², T. Chujo¹²⁰, S.U. Chung⁹⁰,
954 C. Cicalo¹⁰⁰, L. Cifarelli^{12,26}, F. Cindolo⁹⁹, J. Cleymans⁸³, F. Colamaria³¹, D. Colella³¹, A. Collu²³,
955 M. Colocci²⁶, G. Conesa Balbastre⁶⁵, Z. Conesa del Valle⁴⁶, M.E. Connors¹²⁹, J.G. Contreras¹¹,
956 T.M. Cormier¹²⁷, Y. Corrales Morales²⁵, P. Cortese³⁰, I. Cortés Maldonado², M.R. Cosentino¹¹³, F. Costa³⁴,
957 P. Crochet⁶⁴, R. Cruz Albino¹¹, E. Cuautle⁵⁸, L. Cunqueiro⁶⁶, A. Dainese¹⁰², R. Dang⁷, A. Danu⁵⁷, D. Das⁹⁵,
958 I. Das⁴⁶, K. Das⁹⁵, S. Das⁴, A. Dash¹¹⁴, S. Dash⁴⁴, S. De¹²⁴, H. Delagrange^{107,i}, A. Deloff⁷¹, E. Dénes¹²⁸,
959 G. D'Erasmus³¹, A. De Caro^{29,12}, G. de Cataldo⁹⁸, J. de Cuveland³⁹, A. De Falco²³, D. De Gruttola^{29,12},
960 N. De Marco¹⁰⁵, S. De Pasquale²⁹, R. de Rooij⁵², M.A. Diaz Corchero¹⁰, T. Dietel⁴⁹, P. Dillenseger⁴⁸,
961 R. Divià³⁴, D. Di Bari³¹, S. Di Liberto¹⁰³, A. Di Mauro³⁴, P. Di Nezza⁶⁶, Ø. Djuvsland¹⁷, A. Dobrin⁵²,
962 T. Dobrowolski⁷¹, D. Domenicis Gimenez¹¹³, B. Dönigus⁴⁸, O. Dordic²¹, S. Dørheim⁸⁶, A.K. Dubey¹²⁴,
963 A. Dubla⁵², L. Ducroux¹²², P. Dupieux⁶⁴, A.K. Dutta Majumdar⁹⁵, T. E. Hilden⁴², R.J. Ehlers¹²⁹, D. Elia⁹⁸,
964 H. Engel⁴⁷, B. Erazmus^{34,107}, H.A. Erdal³⁵, D. Eschweiler³⁹, B. Espagnon⁴⁶, M. Esposito³⁴, M. Estienne¹⁰⁷,
965 S. Esumi¹²⁰, D. Evans⁹⁶, S. Evdokimov¹⁰⁶, D. Fabris¹⁰², J. Faivre⁶⁵, D. Falchieri²⁶, A. Fantoni⁶⁶, M. Fasel⁸⁷,
966 D. Fehlfker¹⁷, L. Feldkamp⁴⁹, D. Felea⁵⁷, A. Feliciello¹⁰⁵, G. Feofilov¹²³, J. Ferencei⁷⁷, A. Fernández Téllez²,
967 E.G. Ferreira¹⁶, A. Ferretti²⁵, A. Festanti²⁸, J. Figiel¹¹⁰, M.A.S. Figueredo¹¹⁷, S. Filchagin⁹³, D. Finogeev⁵¹,
968 F.M. Fionda³¹, E.M. Fiore³¹, E. Floratos⁸², M. Floris³⁴, S. Foertsch⁶⁰, P. Foka⁹¹, S. Fokin⁹⁴,
969 E. Fragaicomio¹⁰⁴, A. Francescon^{34,28}, U. Frankenfeld⁹¹, U. Fuchs³⁴, C. Furget⁶⁵, M. Fusco Girard²⁹,
970 J.J. Gaardhøje⁷⁴, M. Gagliardi²⁵, A.M. Gago⁹⁷, M. Gallio²⁵, D.R. Gangadharan¹⁹, P. Ganoti⁷⁸,
971 C. Garabatos⁹¹, E. Garcia-Solis¹³, C. Gargiulo³⁴, I. Garishvili⁶⁹, J. Gerhard³⁹, M. Germain¹⁰⁷, A. Gheata³⁴,
972 M. Gheata^{34,57}, B. Ghidini³¹, P. Ghosh¹²⁴, S.K. Ghosh⁴, P. Gianotti⁶⁶, P. Giubellino³⁴,
973 E. Gladysz-Dziadus¹¹⁰, P. Glässel⁸⁷, A. Gomez Ramirez⁴⁷, P. González-Zamora¹⁰, S. Gorbunov³⁹,
974 L. Görlich¹¹⁰, S. Gotovac¹⁰⁹, L.K. Graczykowski¹²⁶, R. Grajcarek⁸⁷, A. Grelli⁵², A. Grigoras³⁴, C. Grigoras³⁴,
975 V. Grigoriev⁷⁰, A. Grigoryan¹, S. Grigoryan⁶¹, B. Grinyov³, N. Grion¹⁰⁴, J.F. Grosse-Oetringhaus³⁴,
976 J.-Y. Grossiord¹²², R. Grosso³⁴, F. Guber⁵¹, R. Guernane⁶⁵, B. Guerzoni²⁶, M. Guilbaud¹²²,
977 K. Gulbrandsen⁷⁴, H. Gulkanyan¹, M. Gumbo⁸³, T. Gunji¹¹⁹, A. Gupta⁸⁴, R. Gupta⁸⁴, K. H. Khan¹⁵,
978 R. Haake⁴⁹, Ø. Haaland¹⁷, C. Hadjidakis⁴⁶, M. Haiduc⁵⁷, H. Hamagaki¹¹⁹, G. Hamar¹²⁸, L.D. Hanratty⁹⁶,
979 A. Hansen⁷⁴, J.W. Harris¹²⁹, H. Hartmann³⁹, A. Harton¹³, D. Hatzifotiadou⁹⁹, S. Hayashi¹¹⁹, S.T. Heckel⁴⁸,
980 M. Heide⁴⁹, H. Helstrup³⁵, A. Herghelegiu^{72,72}, G. Herrera Corral¹¹, B.A. Hess³³, K.F. Hetland³⁵,
981 B. Hippolyte⁵⁰, J. Hladky⁵⁵, P. Hristov³⁴, M. Huang¹⁷, T.J. Humanic¹⁹, N. Hussain⁴¹, D. Hutter³⁹,
982 D.S. Hwang²⁰, R. Ilkaev⁹³, I. Ilkiv⁷¹, M. Inaba¹²⁰, G.M. Innocenti²⁵, C. Ionita³⁴, M. Ippolitov⁹⁴, M. Irfan¹⁸,
983 M. Ivanov⁹¹, V. Ivanov⁷⁹, A. Jacholkowski²⁷, P.M. Jacobs⁶⁸, C. Jahnke¹¹³, H.J. Jang⁶², M.A. Janik¹²⁶,

984 P.H.S.Y. Jayarathna¹¹⁵, C. Jena²⁸, S. Jena¹¹⁵, R.T. Jimenez Bustamante⁵⁸, P.G. Jones⁹⁶, H. Jung⁴⁰, A. Jusko⁹⁶,
 985 V. Kadyshevskiy⁶¹, S. Kalcher³⁹, P. Kalinak^{54,54}, A. Kalweit³⁴, J. Kamin⁴⁸, J.H. Kang¹³⁰, V. Kaplin⁷⁰,
 986 S. Kar¹²⁴, A. Karasu Uysal⁶³, O. Karavichev⁵¹, T. Karavicheva⁵¹, E. Karpechev⁵¹, U. Kebschull⁴⁷,
 987 R. Keidel¹³¹, D.L.D. Keijdener⁵², M.M. Khan^{iii,18}, P. Khan⁹⁵, S.A. Khan¹²⁴, A. Khanzadeev⁷⁹, Y. Kharlov¹⁰⁶,
 988 B. Kileng³⁵, B. Kim¹³⁰, D.W. Kim^{62,40}, D.J. Kim¹¹⁶, J.S. Kim⁴⁰, M. Kim⁴⁰, M. Kim¹³⁰, S. Kim²⁰,
 989 T. Kim¹³⁰, S. Kirsch³⁹, I. Kisel³⁹, S. Kiselev⁵³, A. Kisiel¹²⁶, G. Kiss¹²⁸, J.L. Klay⁶, J. Klein⁸⁷,
 990 C. Klein-Bösing⁴⁹, A. Kluge³⁴, M.L. Knichel⁹¹, A.G. Knospe¹¹¹, C. Kobdaj^{34,108}, M. Kofarago³⁴,
 991 M.K. Köhler⁹¹, T. Kollegger³⁹, A. Kolojvari¹²³, V. Kondratiev¹²³, N. Kondratyeva⁷⁰, A. Konevskikh⁵¹,
 992 V. Kovalenko¹²³, M. Kowalski¹¹⁰, S. Kox⁶⁵, G. Koyithatta Meethalevedu⁴⁴, J. Kral¹¹⁶, I. Králik⁵⁴,
 993 F. Kramer⁴⁸, A. Kravčáková³⁸, M. Krelina³⁷, M. Kretz³⁹, M. Krivda^{96,54}, F. Krizek⁷⁷, E. Kryshen³⁴,
 994 M. Krzewicki⁹¹, V. Kučera⁷⁷, Y. Kucheriaev^{94,i}, T. Kugathasan³⁴, C. Kuhn⁵⁰, P.G. Kuijter⁷⁵, I. Kulakov⁴⁸,
 995 J. Kumar⁴⁴, P. Kurashvili⁷¹, A. Kurepin⁵¹, A.B. Kurepin⁵¹, A. Kuryakin⁹³, S. Kushpil⁷⁷, M.J. Kweon⁸⁷,
 996 Y. Kwon¹³⁰, P. Ladron de Guevara⁵⁸, C. Lagana Fernandes¹¹³, I. Lakomov⁴⁶, R. Langoy¹²⁵, C. Lara⁴⁷,
 997 A. Lardeux¹⁰⁷, A. Lattuca²⁵, S.L. La Pointe⁵², P. La Rocca²⁷, R. Lea^{24,24}, G.R. Lee⁹⁶, I. Legrand³⁴,
 998 J. Lehnert⁴⁸, R.C. Lemmon⁷⁶, V. Lenti⁹⁸, E. Leogrande⁵², M. Leoncino²⁵, I. León Monzón¹¹², P. Lévai¹²⁸,
 999 S. Li^{7,64}, J. Lien¹²⁵, R. Lietava⁹⁶, S. Lindal²¹, V. Lindenstruth³⁹, C. Lippmann⁹¹, M.A. Lisa¹⁹,
 1000 H.M. Ljunggren³², D.F. Lodato⁵², P.I. Loenne¹⁷, V.R. Loggins¹²⁷, V. Loginov⁷⁰, D. Lohner⁸⁷, C. Loizides⁶⁸,
 1001 X. Lopez⁶⁴, E. López Torres⁹, X.-G. Lu⁸⁷, P. Luetig⁴⁸, M. Lunardon²⁸, G. Luparello⁵², R. Ma¹²⁹,
 1002 A. Maevskaya⁵¹, M. Mager³⁴, D.P. Mahapatra⁵⁶, S.M. Mahmood²¹, A. Maire⁸⁷, R.D. Majka¹²⁹, M. Malaev⁷⁹,
 1003 I. Maldonado Cervantes⁵⁸, L. Malinina^{iv,61}, D. Mal'Kevich⁵³, P. Malzacher⁹¹, A. Mamonov⁹³, L. Manceau¹⁰⁵,
 1004 V. Manko⁹⁴, F. Manso⁶⁴, V. Manzari⁹⁸, M. Marchisone^{64,25}, J. Mareš⁵⁵, G.V. Margagliotti²⁴, A. Margotti⁹⁹,
 1005 A. Marín⁹¹, C. Markert¹¹¹, M. Marquard⁴⁸, I. Martashvili¹¹⁸, N.A. Martin⁹¹, P. Martinengo³⁴, M.I. Martínez²,
 1006 G. Martínez García¹⁰⁷, J. Martin Blanco¹⁰⁷, Y. Martynov³, A. Mas¹⁰⁷, S. Masciocchi⁹¹, M. Maserà²⁵,
 1007 A. Masoni¹⁰⁰, L. Massacrier¹⁰⁷, A. Mastroserio³¹, A. Matyja¹¹⁰, C. Mayer¹¹⁰, J. Mazer¹¹⁸, M.A. Mazzoni¹⁰³,
 1008 F. Meddi²², A. Menchaca-Rocha⁵⁹, J. Mercado Pérez⁸⁷, M. Meres³⁶, Y. Miake¹²⁰, K. Mikhaylov^{61,53},
 1009 L. Milano³⁴, J. Milosevic^{v,21}, A. Mischke⁵², A.N. Mishra⁴⁵, D. Miśkowiec⁹¹, J. Mitra¹²⁴, C.M. Mitu⁵⁷,
 1010 J. Mlynar¹²⁷, N. Mohammadi⁵², B. Mohanty^{73,124}, L. Molnar⁵⁰, L. Montaño Zetina¹¹, E. Montes¹⁰,
 1011 M. Morando²⁸, D.A. Moreira De Godoy¹¹³, S. Moretto²⁸, A. Morsch³⁴, V. Muccifora⁶⁶, E. Mudnic¹⁰⁹,
 1012 D. Mühlheim⁴⁹, S. Muhuri¹²⁴, M. Mukherjee¹²⁴, H. Müller³⁴, M.G. Munhoz¹¹³, S. Murray⁸³, L. Musa³⁴,
 1013 J. Musinsky⁵⁴, B.K. Nandi⁴⁴, R. Nania⁹⁹, E. Nappi⁹⁸, C. Nattrass¹¹⁸, K. Nayak⁷³, T.K. Nayak¹²⁴,
 1014 S. Nazarenko⁹³, A. Nedosekin⁵³, M. Nicassio⁹¹, M. Niculescu^{34,57}, B.S. Nielsen⁷⁴, S. Nikolaev⁹⁴,
 1015 S. Nikulin⁹⁴, V. Nikulin⁷⁹, B.S. Nilsen⁸⁰, F. Noferini^{12,99}, P. Nomokonov⁶¹, G. Nooren⁵², J. Norman¹¹⁷,
 1016 A. Nyanin⁹⁴, J. Nystrand¹⁷, H. Oeschler⁸⁷, S. Oh¹²⁹, S.K. Oh^{vi,40}, A. Okatan⁶³, L. Olah¹²⁸, J. Oleniacz¹²⁶,
 1017 A.C. Oliveira Da Silva¹¹³, J. Onderwaater⁹¹, C. Oppedisano¹⁰⁵, A. Ortiz Velasquez³², G. Ortona²⁵,
 1018 A. Oskarsson³², J. Otwinowski⁹¹, K. Oyama⁸⁷, P. Sahoo⁴⁵, Y. Pachmayer⁸⁷, M. Pachr³⁷, P. Pagano²⁹,
 1019 G. Paic⁵⁸, F. Painke³⁹, C. Pajares¹⁶, S.K. Pal¹²⁴, A. Palmeri¹⁰¹, D. Pant⁴⁴, V. Papikyan¹, G.S. Pappalardo¹⁰¹,
 1020 P. Pareek⁴⁵, W.J. Park⁹¹, S. Parmar⁸¹, A. Passfeld⁴⁹, D.I. Patalakha¹⁰⁶, V. Paticchio⁹⁸, B. Paul⁹⁵, T. Pawlak¹²⁶,
 1021 T. Peitzmann⁵², H. Pereira Da Costa¹⁴, E. Pereira De Oliveira Filho¹¹³, D. Peresunko⁹⁴, C.E. Pérez Lara⁷⁵,
 1022 A. Pesci⁹⁹, V. Peskov⁴⁸, Y. Pestov⁵, V. Petráček³⁷, M. Petran³⁷, M. Petris⁷², M. Petrovici⁷², C. Petta²⁷,
 1023 S. Piano¹⁰⁴, M. Pikna³⁶, P. Pillot¹⁰⁷, O. Pinazza^{99,34}, L. Pinsky¹¹⁵, D.B. Piyarathna¹¹⁵, M. Płoskoń⁶⁸,
 1024 M. Planinic^{121,92}, J. Pluta¹²⁶, S. Pochybova¹²⁸, P.L.M. Podesta-Lerma¹¹², M.G. Poghosyan³⁴,
 1025 E.H.O. Pohjoisaho⁴², B. Polichtchouk¹⁰⁶, N. Poljak⁹², A. Pop⁷², S. Porteboeuf-Houssais⁶⁴, J. Porter⁶⁸,
 1026 B. Potukuchi⁸⁴, S.K. Prasad¹²⁷, R. Preghenella^{99,12}, F. Prino¹⁰⁵, C.A. Pruneau¹²⁷, I. Pshenichnov⁵¹,
 1027 G. Puudu²³, P. Pujahari¹²⁷, V. Punin⁹³, J. Putschke¹²⁷, H. Qvigstad²¹, A. Rachevski¹⁰⁴, S. Raha⁴, J. Rak¹¹⁶,
 1028 A. Rakotozafindrabe¹⁴, L. Ramello³⁰, R. Raniwala⁸⁵, S. Raniwala⁸⁵, S.S. Räsänen⁴², B.T. Rascanu⁴⁸,
 1029 D. Rathee⁸¹, A.W. Rauf¹⁵, V. Razazi²³, K.F. Read¹¹⁸, J.S. Real⁶⁵, K. Redlich^{vii,71}, R.J. Reed¹²⁹,
 1030 A. Rehman¹⁷, P. Reichelt⁴⁸, M. Reicher⁵², F. Reidt³⁴, R. Renfordt⁴⁸, A.R. Reolon⁶⁶, A. Reshetin⁵¹,
 1031 F. Rettig³⁹, J.-P. Revol³⁴, K. Reygers⁸⁷, V. Riabov⁷⁹, R.A. Ricci⁶⁷, T. Richert³², M. Richter²¹, P. Riedler³⁴,
 1032 W. Riegler³⁴, F. Riggi²⁷, A. Rivetti¹⁰⁵, E. Rocco⁵², M. Rodríguez Cahuantzi², A. Rodríguez Manso⁷⁵,
 1033 K. Røed²¹, E. Rogochaya⁶¹, S. Rohni⁸⁴, D. Rohr³⁹, D. Röhrich¹⁷, R. Romita⁷⁶, F. Ronchetti⁶⁶,
 1034 L. Ronflette¹⁰⁷, P. Rosnet⁶⁴, A. Rossi³⁴, F. Roukoutakis⁸², A. Roy⁴⁵, C. Roy⁵⁰, P. Roy⁹⁵,
 1035 A.J. Rubio Montero¹⁰, R. Rui²⁴, R. Russo²⁵, E. Ryabinkin⁹⁴, Y. Ryabov⁷⁹, A. Rybicki¹¹⁰, S. Sadovsky¹⁰⁶,
 1036 K. Šafařík³⁴, B. Sahlmüller⁴⁸, R. Sahoo⁴⁵, P.K. Sahu⁵⁶, J. Saini¹²⁴, S. Sakai⁶⁸, C.A. Salgado¹⁶, J. Salzwedel¹⁹,
 1037 S. Sambyal⁸⁴, V. Samsonov⁷⁹, X. Sanchez Castro⁵⁰, F.J. Sánchez Rodríguez¹¹², L. Šándor⁵⁴, A. Sandoval⁵⁹,
 1038 M. Sano¹²⁰, G. Santagati²⁷, D. Sarkar¹²⁴, E. Scapparone⁹⁹, F. Scarlassara²⁸, R.P. Scharenberg⁸⁹, C. Schiaua⁷²,
 1039 R. Schicker⁸⁷, C. Schmidt⁹¹, H.R. Schmidt³³, S. Schuchmann⁴⁸, J. Schukraft³⁴, M. Schulc³⁷, T. Schuster¹²⁹,

1040 Y. Schutz^{107,34}, K. Schwarz⁹¹, K. Schweda⁹¹, G. Scioli²⁶, E. Scomparin¹⁰⁵, R. Scott¹¹⁸, G. Segato²⁸,
 1041 J.E. Seger⁸⁰, Y. Sekiguchi¹¹⁹, I. Selyuzhenkov⁹¹, J. Seo⁹⁰, E. Serradilla^{10,59}, A. Sevcenco⁵⁷, A. Shabetai¹⁰⁷,
 1042 G. Shabratova⁶¹, R. Shahoyan³⁴, A. Shangaraev¹⁰⁶, N. Sharma¹¹⁸, S. Sharma⁸⁴, K. Shigaki⁴³, K. Shtejer²⁵,
 1043 Y. Sibiriyak⁹⁴, S. Siddhanta¹⁰⁰, T. Siemiarczuk⁷¹, D. Silvermyr⁷⁸, C. Silvestre⁶⁵, G. Simatovic¹²¹,
 1044 R. Singaraju¹²⁴, R. Singh⁸⁴, S. Singha^{124,73}, V. Singhal¹²⁴, B.C. Sinha¹²⁴, T. Sinha⁹⁵, B. Sitar³⁶, M. Sitta³⁰,
 1045 T.B. Skaali²¹, K. Skjerdal¹⁷, M. Slupecki¹¹⁶, N. Smirnov¹²⁹, R.J.M. Snellings⁵², C. Sogaard³², R. Soltz⁶⁹,
 1046 J. Song⁹⁰, M. Song¹³⁰, F. Soramel²⁸, S. Sorensen¹¹⁸, M. Spacek³⁷, E. Spiriti⁶⁶, I. Sputowska¹¹⁰,
 1047 M. Spyropoulou-Stassinaki⁸², B.K. Srivastava⁸⁹, J. Stachel⁸⁷, I. Stan⁵⁷, G. Stefanek⁷¹, M. Steinpreis¹⁹,
 1048 E. Stenlund³², G. Steyn⁶⁰, J.H. Stiller⁸⁷, D. Stocco¹⁰⁷, M. Stolpovskiy¹⁰⁶, P. Strmen³⁶, A.A.P. Suaide¹¹³,
 1049 T. Sugitate⁴³, C. Suire⁴⁶, M. Suleymanov¹⁵, R. Sultanov⁵³, M. Šumbera⁷⁷, T. Susa⁹², T.J.M. Symons⁶⁸,
 1050 A. Szabo³⁶, A. Szanto de Toledo¹¹³, I. Szarka³⁶, A. Szczepankiewicz³⁴, M. Szymanski¹²⁶, J. Takahashi¹¹⁴,
 1051 M.A. Tangaro³¹, J.D. Tapia Takaki^{viii.46}, A. Tarantola Peloni⁴⁸, A. Tarazona Martinez³⁴, M.G. Tarzila⁷²,
 1052 A. Tauro³⁴, G. Tejada Muñoz², A. Telesca³⁴, C. Terrevoli²³, J. Thäder⁹¹, D. Thomas⁵², R. Tieulent¹²²,
 1053 A.R. Timmins¹¹⁵, A. Toia¹⁰², V. Trubnikov³, W.H. Trzaska¹¹⁶, T. Tsuji¹¹⁹, A. Tumkin⁹³, R. Turrisi¹⁰²,
 1054 T.S. Tveter²¹, K. Ullaland¹⁷, A. Uras¹²², G.L. Usai²³, M. Vajzer⁷⁷, M. Vala^{54,61}, L. Valencia Palomo⁶⁴,
 1055 S. Vallero⁸⁷, P. Vande Vyvre³⁴, J. Van Der Maarel⁵², J.W. Van Hoorne³⁴, M. van Leeuwen⁵², A. Vargas²,
 1056 M. Vargyas¹¹⁶, R. Varma⁴⁴, M. Vasileiou⁸², A. Vasiliev⁹⁴, V. Vechernin¹²³, M. Veldhoen⁵², A. Velure¹⁷,
 1057 M. Venaruzzo^{24,67}, E. Vercellin²⁵, S. Vergara Limón², R. Vernet⁸, M. Verweij¹²⁷, L. Vickovic¹⁰⁹, G. Viesti²⁸,
 1058 J. Viinikainen¹¹⁶, Z. Vilakazi⁶⁰, O. Villalobos Baillie⁹⁶, A. Vinogradov⁹⁴, L. Vinogradov¹²³, Y. Vinogradov⁹³,
 1059 T. Virgili²⁹, Y.P. Viyogi¹²⁴, A. Vodopyanov⁶¹, M.A. Völkl⁸⁷, K. Voloshin⁵³, S.A. Voloshin¹²⁷, G. Volpe³⁴,
 1060 B. von Haller³⁴, I. Vorobyev¹²³, D. Vranic^{91,34}, J. Vrláková³⁸, B. Vulpescu⁶⁴, A. Vyushin⁹³, B. Wagner¹⁷,
 1061 J. Wagner⁹¹, V. Wagner³⁷, M. Wang^{7,107}, Y. Wang⁸⁷, D. Watanabe¹²⁰, M. Weber¹¹⁵, J.P. Wessels⁴⁹,
 1062 U. Westerhoff⁴⁹, J. Wiechula³³, J. Wikne²¹, M. Wilde⁴⁹, G. Wilk⁷¹, J. Wilkinson⁸⁷, M.C.S. Williams⁹⁹,
 1063 B. Windelband⁸⁷, M. Winn⁸⁷, C.G. Yaldo¹²⁷, Y. Yamaguchi¹¹⁹, H. Yang⁵², P. Yang⁷, S. Yang¹⁷, S. Yano⁴³,
 1064 S. Yasnopolskiy⁹⁴, J. Yi⁹⁰, Z. Yin⁷, I.-K. Yoo⁹⁰, I. Yushmanov⁹⁴, V. Zaccaro⁷⁴, C. Zach³⁷, A. Zaman¹⁵,
 1065 C. Zampolli⁹⁹, S. Zaporozhets⁶¹, A. Zarochentsev¹²³, P. Závada⁵⁵, N. Zaviyalov⁹³, H. Zbroszczyk¹²⁶,
 1066 I.S. Zgura⁵⁷, M. Zhalov⁷⁹, H. Zhang⁷, X. Zhang^{68,7}, Y. Zhang⁷, C. Zhao²¹, N. Zhigareva⁵³, D. Zhou⁷,
 1067 F. Zhou⁷, Y. Zhou⁵², Zhou, Zhuo¹⁷, H. Zhu⁷, J. Zhu⁷, X. Zhu⁷, A. Zichichi^{12,26}, A. Zimmermann⁸⁷,
 1068 M.B. Zimmermann^{34,49}, G. Zinovjev³, Y. Zoccarato¹²², M. Zyzak⁴⁸

Affiliation notes

- 1069 ⁱ Deceased
 1070 ⁱⁱ Also at: St. Petersburg State Polytechnical University
 1071 ⁱⁱⁱ Also at: Department of Applied Physics, Aligarh Muslim University, Aligarh, India
 1072 ^{iv} Also at: M.V. Lomonosov Moscow State University, D.V. Skobeltsyn Institute of Nuclear Physics,
 1073 Moscow, Russia
 1074 ^v Also at: University of Belgrade, Faculty of Physics and "Vinča" Institute of Nuclear Sciences, Belgrade,
 1075 Serbia
 1076 ^{vi} Permanent Address: Permanent Address: Konkuk University, Seoul, Korea
 1077 ^{vii} Also at: Institute of Theoretical Physics, University of Wrocław, Wrocław, Poland
 1078 ^{viii} Also at: University of Kansas, Lawrence, KS, United States
 1079

Collaboration Institutes

- 1080 ¹ A.I. Alikhanyan National Science Laboratory (Yerevan Physics Institute) Foundation, Yerevan, Armenia
 1081 ² Benemérita Universidad Autónoma de Puebla, Puebla, Mexico
 1082 ³ Bogolyubov Institute for Theoretical Physics, Kiev, Ukraine
 1083 ⁴ Bose Institute, Department of Physics and Centre for Astroparticle Physics and Space Science (CAPSS),
 1084 Kolkata, India
 1085 ⁵ Budker Institute for Nuclear Physics, Novosibirsk, Russia
 1086 ⁶ California Polytechnic State University, San Luis Obispo, CA, United States
 1087 ⁷ Central China Normal University, Wuhan, China
 1088 ⁸ Centre de Calcul de l'IN2P3, Villeurbanne, France
 1089 ⁹ Centro de Aplicaciones Tecnológicas y Desarrollo Nuclear (CEADEN), Havana, Cuba
 1090 ¹⁰ Centro de Investigaciones Energéticas Medioambientales y Tecnológicas (CIEMAT), Madrid, Spain
 1091 ¹¹ Centro de Investigación y de Estudios Avanzados (CINVESTAV), Mexico City and Mérida, Mexico
 1092

- 1093 12 Centro Fermi - Museo Storico della Fisica e Centro Studi e Ricerche “Enrico Fermi”, Rome, Italy
- 1094 13 Chicago State University, Chicago, USA
- 1095 14 Commissariat à l’Energie Atomique, IRFU, Saclay, France
- 1096 15 COMSATS Institute of Information Technology (CIIT), Islamabad, Pakistan
- 1097 16 Departamento de Física de Partículas and IGFAE, Universidad de Santiago de Compostela, Santiago de Compostela, Spain
- 1098
- 1099 17 Department of Physics and Technology, University of Bergen, Bergen, Norway
- 1100 18 Department of Physics, Aligarh Muslim University, Aligarh, India
- 1101 19 Department of Physics, Ohio State University, Columbus, OH, United States
- 1102 20 Department of Physics, Sejong University, Seoul, South Korea
- 1103 21 Department of Physics, University of Oslo, Oslo, Norway
- 1104 22 Dipartimento di Fisica dell’Università ‘La Sapienza’ and Sezione INFN Rome, Italy
- 1105 23 Dipartimento di Fisica dell’Università and Sezione INFN, Cagliari, Italy
- 1106 24 Dipartimento di Fisica dell’Università and Sezione INFN, Trieste, Italy
- 1107 25 Dipartimento di Fisica dell’Università and Sezione INFN, Turin, Italy
- 1108 26 Dipartimento di Fisica e Astronomia dell’Università and Sezione INFN, Bologna, Italy
- 1109 27 Dipartimento di Fisica e Astronomia dell’Università and Sezione INFN, Catania, Italy
- 1110 28 Dipartimento di Fisica e Astronomia dell’Università and Sezione INFN, Padova, Italy
- 1111 29 Dipartimento di Fisica ‘E.R. Caianiello’ dell’Università and Gruppo Collegato INFN, Salerno, Italy
- 1112 30 Dipartimento di Scienze e Innovazione Tecnologica dell’Università del Piemonte Orientale and Gruppo Collegato INFN, Alessandria, Italy
- 1113
- 1114 31 Dipartimento Interateneo di Fisica ‘M. Merlin’ and Sezione INFN, Bari, Italy
- 1115 32 Division of Experimental High Energy Physics, University of Lund, Lund, Sweden
- 1116 33 Eberhard Karls Universität Tübingen, Tübingen, Germany
- 1117 34 European Organization for Nuclear Research (CERN), Geneva, Switzerland
- 1118 35 Faculty of Engineering, Bergen University College, Bergen, Norway
- 1119 36 Faculty of Mathematics, Physics and Informatics, Comenius University, Bratislava, Slovakia
- 1120 37 Faculty of Nuclear Sciences and Physical Engineering, Czech Technical University in Prague, Prague, Czech Republic
- 1121
- 1122 38 Faculty of Science, P.J. Šafárik University, Košice, Slovakia
- 1123 39 Frankfurt Institute for Advanced Studies, Johann Wolfgang Goethe-Universität Frankfurt, Frankfurt, Germany
- 1124
- 1125 40 Gangneung-Wonju National University, Gangneung, South Korea
- 1126 41 Gauhati University, Department of Physics, Guwahati, India
- 1127 42 Helsinki Institute of Physics (HIP), Helsinki, Finland
- 1128 43 Hiroshima University, Hiroshima, Japan
- 1129 44 Indian Institute of Technology Bombay (IIT), Mumbai, India
- 1130 45 Indian Institute of Technology Indore, Indore (IITI), India
- 1131 46 Institut de Physique Nucléaire d’Orsay (IPNO), Université Paris-Sud, CNRS-IN2P3, Orsay, France
- 1132 47 Institut für Informatik, Johann Wolfgang Goethe-Universität Frankfurt, Frankfurt, Germany
- 1133 48 Institut für Kernphysik, Johann Wolfgang Goethe-Universität Frankfurt, Frankfurt, Germany
- 1134 49 Institut für Kernphysik, Westfälische Wilhelms-Universität Münster, Münster, Germany
- 1135 50 Institut Pluridisciplinaire Hubert Curien (IPHC), Université de Strasbourg, CNRS-IN2P3, Strasbourg, France
- 1136
- 1137 51 Institute for Nuclear Research, Academy of Sciences, Moscow, Russia
- 1138 52 Institute for Subatomic Physics of Utrecht University, Utrecht, Netherlands
- 1139 53 Institute for Theoretical and Experimental Physics, Moscow, Russia
- 1140 54 Institute of Experimental Physics, Slovak Academy of Sciences, Košice, Slovakia
- 1141 55 Institute of Physics, Academy of Sciences of the Czech Republic, Prague, Czech Republic
- 1142 56 Institute of Physics, Bhubaneswar, India
- 1143 57 Institute of Space Science (ISS), Bucharest, Romania
- 1144 58 Instituto de Ciencias Nucleares, Universidad Nacional Autónoma de México, Mexico City, Mexico
- 1145 59 Instituto de Física, Universidad Nacional Autónoma de México, Mexico City, Mexico
- 1146 60 iThemba LABS, National Research Foundation, Somerset West, South Africa
- 1147 61 Joint Institute for Nuclear Research (JINR), Dubna, Russia
- 1148 62 Korea Institute of Science and Technology Information, Daejeon, South Korea

- 1149 63 KTO Karatay University, Konya, Turkey
1150 64 Laboratoire de Physique Corpusculaire (LPC), Clermont Université, Université Blaise Pascal,
1151 CNRS–IN2P3, Clermont-Ferrand, France
1152 65 Laboratoire de Physique Subatomique et de Cosmologie, Université Grenoble-Alpes, CNRS-IN2P3,
1153 Grenoble, France
1154 66 Laboratori Nazionali di Frascati, INFN, Frascati, Italy
1155 67 Laboratori Nazionali di Legnaro, INFN, Legnaro, Italy
1156 68 Lawrence Berkeley National Laboratory, Berkeley, CA, United States
1157 69 Lawrence Livermore National Laboratory, Livermore, CA, United States
1158 70 Moscow Engineering Physics Institute, Moscow, Russia
1159 71 National Centre for Nuclear Studies, Warsaw, Poland
1160 72 National Institute for Physics and Nuclear Engineering, Bucharest, Romania
1161 73 National Institute of Science Education and Research, Bhubaneswar, India
1162 74 Niels Bohr Institute, University of Copenhagen, Copenhagen, Denmark
1163 75 Nikhef, National Institute for Subatomic Physics, Amsterdam, Netherlands
1164 76 Nuclear Physics Group, STFC Daresbury Laboratory, Daresbury, United Kingdom
1165 77 Nuclear Physics Institute, Academy of Sciences of the Czech Republic, Řež u Prahy, Czech Republic
1166 78 Oak Ridge National Laboratory, Oak Ridge, TN, United States
1167 79 Petersburg Nuclear Physics Institute, Gatchina, Russia
1168 80 Physics Department, Creighton University, Omaha, NE, United States
1169 81 Physics Department, Panjab University, Chandigarh, India
1170 82 Physics Department, University of Athens, Athens, Greece
1171 83 Physics Department, University of Cape Town, Cape Town, South Africa
1172 84 Physics Department, University of Jammu, Jammu, India
1173 85 Physics Department, University of Rajasthan, Jaipur, India
1174 86 Physik Department, Technische Universität München, Munich, Germany
1175 87 Physikalisches Institut, Ruprecht-Karls-Universität Heidelberg, Heidelberg, Germany
1176 88 Politecnico di Torino, Turin, Italy
1177 89 Purdue University, West Lafayette, IN, United States
1178 90 Pusan National University, Pusan, South Korea
1179 91 Research Division and ExtreMe Matter Institute EMMI, GSI Helmholtzzentrum für
1180 Schwerionenforschung, Darmstadt, Germany
1181 92 Rudjer Bošković Institute, Zagreb, Croatia
1182 93 Russian Federal Nuclear Center (VNIIEF), Sarov, Russia
1183 94 Russian Research Centre Kurchatov Institute, Moscow, Russia
1184 95 Saha Institute of Nuclear Physics, Kolkata, India
1185 96 School of Physics and Astronomy, University of Birmingham, Birmingham, United Kingdom
1186 97 Sección Física, Departamento de Ciencias, Pontificia Universidad Católica del Perú, Lima, Peru
1187 98 Sezione INFN, Bari, Italy
1188 99 Sezione INFN, Bologna, Italy
1189 100 Sezione INFN, Cagliari, Italy
1190 101 Sezione INFN, Catania, Italy
1191 102 Sezione INFN, Padova, Italy
1192 103 Sezione INFN, Rome, Italy
1193 104 Sezione INFN, Trieste, Italy
1194 105 Sezione INFN, Turin, Italy
1195 106 SSC IHEP of NRC Kurchatov institute, Protvino, Russia
1196 107 SUBATECH, Ecole des Mines de Nantes, Université de Nantes, CNRS-IN2P3, Nantes, France
1197 108 Suranaree University of Technology, Nakhon Ratchasima, Thailand
1198 109 Technical University of Split FESB, Split, Croatia
1199 110 The Henryk Niewodniczanski Institute of Nuclear Physics, Polish Academy of Sciences, Cracow, Poland
1200 111 The University of Texas at Austin, Physics Department, Austin, TX, USA
1201 112 Universidad Autónoma de Sinaloa, Culiacán, Mexico
1202 113 Universidade de São Paulo (USP), São Paulo, Brazil
1203 114 Universidade Estadual de Campinas (UNICAMP), Campinas, Brazil
1204 115 University of Houston, Houston, TX, United States

-
- 1205 ¹¹⁶ University of Jyväskylä, Jyväskylä, Finland
1206 ¹¹⁷ University of Liverpool, Liverpool, United Kingdom
1207 ¹¹⁸ University of Tennessee, Knoxville, TN, United States
1208 ¹¹⁹ University of Tokyo, Tokyo, Japan
1209 ¹²⁰ University of Tsukuba, Tsukuba, Japan
1210 ¹²¹ University of Zagreb, Zagreb, Croatia
1211 ¹²² Université de Lyon, Université Lyon 1, CNRS/IN2P3, IPN-Lyon, Villeurbanne, France
1212 ¹²³ V. Fock Institute for Physics, St. Petersburg State University, St. Petersburg, Russia
1213 ¹²⁴ Variable Energy Cyclotron Centre, Kolkata, India
1214 ¹²⁵ Vestfold University College, Tonsberg, Norway
1215 ¹²⁶ Warsaw University of Technology, Warsaw, Poland
1216 ¹²⁷ Wayne State University, Detroit, MI, United States
1217 ¹²⁸ Wigner Research Centre for Physics, Hungarian Academy of Sciences, Budapest, Hungary
1218 ¹²⁹ Yale University, New Haven, CT, United States
1219 ¹³⁰ Yonsei University, Seoul, South Korea
1220 ¹³¹ Zentrum für Technologietransfer und Telekommunikation (ZTT), Fachhochschule Worms, Worms,
1221 Germany